Natural variation in salt-induced changes in root:shoot ratio reveals SR3G as a negative regulator of root suberization and salt resilience in Arabidopsis

Maryam Rahmati Ishka[1], - ORCID - 0000-0002-5447-643X - mri23@cornell.edu

Hayley Sussman[1], - ORCID - 0000-0002-1331-3319 - hs995@cornell.edu

Yunfei Hu[2], - ORCID - 0009-0004 -9799-7798 - huyf19@lzu.edu.cn

Mashael Daghash Alqahtani[3], - ORCID - 0000-0003-0043-0847 - mdalqahtani@pnu.edu.sa

Eric Craft[4], - ORCID - 0000-0003-0966-8296 - ejc35@cornell.edu

Ronell Sicat[5], - ORCID - 0000-0001-7037-1614 - ronell.sicat@kaust.edu.sa

Minmin Wang[6], - ORCID - 0000-0001-9545-7895 - minwang@ucdavis.edu

Li'ang Yu[1], - ORCID - 0000-0002-9556-011X - ly76@cornell.edu

Rashid Ait-Haddou[5, 6], - ORCID – 0000-0002-2606-127X – rachid.aithaddou@kfupm.edu.sa

Bo Li[2] - ORCID - 0000-0002-3603-3352 - li_bo@lzu.edu.cn

Georgia Drakakaki[7], - ORCID – 0000-0002-3949-8657 - gdrakakaki@ucdavis.edu

Andrew Nelson[1], - ORCID - 0000-0001-9896-1739 - an425@cornell.edu

Miguel Pineros[4], ORCID - 0000-0002-7166-1848 - map25@cornell.edu

Arthur Korte[8], - ORCID - 0000-0003-0831-1463 - arthur.korte@uni-wuerzburg.de

Lukasz Jaremko[9], lukasz.jaremko@kaust.edu.sa

Christa Testerink[10], - ORCID - 0000-0001-6738-115X - christa.testerink@wur.nl

Mark Tester[3], - ORCID - 0000-0002-5085-8801 mark.tester@kaust.edu.sa

Magdalena M. Julkowska[1,3]* - ORCID - 0000-0002-4259-8296

*- Corresponding author mmj55@cornell.edu

Affiliations:
1 - Boyce Thompson Institute, Ithaca, NY, USA
2 - Lanzhou University, Lanzhou, China
3 - Center for Desert Agriculture, King Abdullah University of Science and Technology, Thuwal, Saudi Arabia
4 - USDA-ARS, Ithaca, NY, USA
5 - Visualization Core Lab, King Abdullah University of Science and Technology, Thuwal, Saudi Arabia
6 - King Fahd University of Petroleum and Minerals, Department of Mathematics
7 - UC Davis, Davis, CA, USA
8 - Julius-von-Sachs-Institute & Center for Computational and Theoretical Biology, JMU, Wuerzburg, Germany
9 - King Abdullah University of Science and Technology, Thuwal, Saudi Arabia
10 - Wageningen Research and University, Wageningen, The Netherlands

Abstract

Soil salinity is one of the major threats to agricultural productivity worldwide. Salt stress exposure alters root and shoot growth rates, thereby affecting overall plant performance. While past studies have extensively documented the effect of salt stress on root elongation and shoot development separately, here we take an innovative approach by examining the coordination of root and shoot growth under salt stress conditions. Utilizing a newly developed tool for quantifying the root:shoot ratio in agar-grown Arabidopsis seedlings, we found that salt stress results in a loss of coordination between root and shoot growth rates. We identify a specific gene cluster encoding domain-of-unknown-function 247 (DUF247), and characterize one of these genes as Salt Root:shoot Ratio Regulator Gene (SR3G). Further analysis elucidates the role of SR3G as a negative regulator of salt stress tolerance, revealing its function in regulating shoot growth, root suberization, and sodium accumulation. We further characterize that *SR3G* expression is modulated by *WRKY75* transcription factor, known as a positive regulator of salt stress tolerance. Finally, we show that the salt stress sensitivity of *wrky75* mutant is completely diminished when it is combined with *sr3g* mutation. Together, our results demonstrate that utilizing root:shoot ratio as an architectural feature leads to the discovery of new stress resilience gene. The study's innovative approach and findings not only contribute to our understanding of plant stress tolerance mechanisms but also open new avenues for genetic and agronomic strategies to enhance crop environmental resilience.

Introduction

Salt stress is predominant in the dryland areas where evaporation rate exceeds water input. As all water contains dissolved ions, the prolonged exposure to drought stress results in increased accumulation of salts in the upper soil layers (Abrol et al., 1988; Fischer et al., 2021; Richards, 1969). Dryland areas of South America, southern and western Australia, Mexico, southwest United States, and South Africa were previously identified as primary hotspots for soil salinization (Hassani et al., 2021). As fresh water becomes scarcer, understanding the mechanisms of salt stress resilience becomes of paramount importance in the context of global agricultural productivity and sustainability.

Salt stress detrimentally affects plant growth and development, decreasing the activity of the meristem (West et al., 2004). Studies utilizing main root elongation as an indicator of salt tolerance have led to identification of many crucial components of salt stress signaling and tolerance, including genes involved in salt-overly sensitive signaling (SOS) pathway, jasmonate , ethylene, abscisic acid (ABA), and reactive oxygen species (ROS) in glycophytes and halophytes alike (Fu et al., 2019; Geng et al., 2013; Hu et al., 2023; Şekerci et al., 2023; Valenzuela et al., 2016; Wu et al., 1996). Additionally, negative halotropism response, that describes a directional growth of main root away from the salt gradient, was used to identify a wide range of molecular components regulating the auxin redistribution and cell-wall remodeling, to actively avoid high salt (Deolu-Ajayi et al., 2019; Galvan-Ampudia et al., 2013; Korver et al., 2020; Yu et al., 2022; Y. Zou et al., 2022). The development of lateral roots is affected by salinity, and the differential effect on main and lateral roots within specific genotype can result in substantial reprogramming of root system architecture (Julkowska et al., 2017, 2014). The shoot development is impacted by salt stress, as the salt impacts the plant transpiration and photosynthetic efficiency instantaneously (Awlia et al., 2021, 2016; Julkowska et al., 2016). Many forward genetic studies were highly successful in associating natural variation in root and shoot growth with allelic variation in gene coding and promoter regions, thereby identifying potential new target traits for improved stress resilience (Awlia et al., 2021; Julkowska et al., 2017, 2016). However, these studies typically focus on either above or below ground tissue.

The coordination of root and shoot growth rate is an important aspect of seedling establishment, and becomes even more critical under abiotic stress (Bacher et al., 2022; Chen et al., 2022; Karcher et al., 2008; Wang et al., 2018; Xu et al., 2015). The importance of increased root:shoot ratio, maximizing water scavenging while limiting transpiration, is well studied under drought stress (Asch et al., 2005; Chen et al., 2022; Karcher et al., 2008; Uga et al., 2013). However, the effect of salt stress on root:shoot ratio is yet to be described, and its contribution to salt stress remains unknown. Here, we developed a tool to quantify root:shoot ratio from agar-grown Arabidopsis seedlings, and re-analyzed the natural diversity panel of Arabidopsis exposed to salt stress (Julkowska et al., 2017). We have observed that while salt stress does not elicit a clear response in root:shoot ratio, it results in loss of coordination of root and shoot growth rates. The locus associated with salt-induced changes in root:shoot ratio consisted of a gene cluster encoding domain-of-unknown-function 247 (DUF247), with majority of SNPs clustering into one specific gene (At3g50160), that we named as Salt Root:shoot Ratio Regulator Gene (SR3G). Further characterization of SR3G revealed its function as a negative regulator of salt stress resilience, through regulation of root suberization, shoot growth, and Na^+ accumulation. We found WRKY75 transcription factor, a positive regulator of salt stress tolerance, acts upstream of SR3G, binding directly to the SR3G promoter in yeast. While *sr3g* and *wrky75* mutants showed contrasting salt stress response, the double mutants of *sr3g/wrky75* displayed reduced sensitivity to salt stress.

Materials & Methods

Screening HapMap population for the increase in root and shoot size

The images collected within (Julkowska et al., 2017) were re-analyzed in this manuscript to examine salt-induced changes in the root:shoot ratio for the data presented here. 360 accessions of the Arabidopsis HapMap population (Weigel and Mott, 2009) were screened over 7 experimental batches, using 4 biological replicates per genotype per condition. The seeds were surface sterilized, incubated in sterile MQ water at 4°C for 48 h, and germinated on media containing ½ Murashige-Skoog, 0.5% sucrose, 0.1% MES buffer, pH 5.8 (KOH) and 1% Dashin agar. The 4-day-old seedlings were subsequently transferred to media additionally supplemented with 0, 75 or 125 mM NaCl. The plates were scanned every 2nd day using a flat-bed scanner for 8 consecutive days.

The collected images were analyzed for green and white pixels, corresponding to the projected surface of the shoot and root, respectively (https://github.com/ronellsicat/PlantSeg). A Matlab-based tool was developed to simplify and speed up the segmentation and analysis pipeline. For automatic segmentation, the tool uses a combination of image operations (histogram equalization), thresholding on different color spaces (e.g., RGB, YCbCr, Lab, HSV), and binary image processing (boundary and islands removal). As the tool is digitalizing various color scales and classifies pixels into either white (root), green (shoot) or blue (background) categories, the adjustment for white balance is obsolete. For analysis, the tool uses connected components analysis to extract the plants (combined roots and shoots) and can guide the user to find possible mistakes which can be manually corrected via the user interface. After segmentation, the number of pixels for roots and shoots are counted and recorded automatically. More details are provided in the publicly available repository for the tool (https://github.com/ronellsicat/PlantSeg). The collected images and corresponding data acquired from them using the tool can be accessed at Zenodo Repository (experimental batch 1: https://doi.org/10.5281/zenodo.7272155; experimental batch 2: https://doi.org/10.5281/zenodo.7272344; experimental batch 3: https://doi.org/10.5281/zenodo.7272647; experimental batch 4: https://doi.org/10.5281/zenodo.7271841; experimental batch 5: https://doi.org/10.5281/zenodo.7272139; experimental batch 6: https://doi.org/10.5281/zenodo.7273936; experimental batch 7: https://doi.org/10.5281/zenodo.7273937; quantified data: https://doi.org/10.5281/zenodo.7268673). The tool's precision was evaluated by growing the Col-0 seedlings on agar plates, analyzing their root and shoot projected area on the final day using the tool, and correlating it with the recorded fresh and dry weight of the seedlings (**Fig. S1**). The collected data from the HapMap panel was analyzed using R for potential outliers (samples identified to be more than 3x standard deviation from the mean of each genotype within each condition), and the genotype-specific mean was calculated using the stats package (Team et al., 2018). The overall increase in root and shoot area was investigated for differences between control and salt stress conditions (**Fig. S2**). The root and shoot growth were estimated by fitting a linear function for a log-transformed projected root or shoot area over the non-transformed timeline of the experiment (https://rpubs.com/mjulkowska/HapMap-root-shoot-data). The data were subsequently used to explore differences between the experimental batches and the standard deviations within individual accessions. The genotypes above 3 standard deviations from the population's mean were excluded from further analysis. The salt tolerance index (STI) was calculated for root and shoot growth by dividing the average trait value at salt stress by the genotype-specific average at control conditions (**Fig. S3**). The correlations between individual traits were examined using the genotypic mean (**Fig. S4**). All quantitative data for root and shoot growth was visualized using ggplot2, corrplot and ggpubr packages

143 (Kassambara, n.d.; Wei and Simko, 2017; Wilke, 2016). For all measured traits, we estimated broad sense
144 heritability (H^2) using the MVApp (Julkowska et al., 2018) (**Table S1**). The data used as an input for GWAS
145 can be found in **Table S2**.

146 **Genome-Wide Association Study**

147 The genotype-specific mean was used as an input to GWAS. The GWAS was conducted as described in
148 (Awlia et al., 2021), initially using 250 k SNPs (Horton et al., 2012) and subsequently using 4 M SNPs
149 (1001genomes.org). The GWAS associations were evaluated for minor allele count (MAC) and association
150 strength above the Bonferroni threshold with -log10(p-value/#SNPs), calculated for each sub-population
151 of SNPs above threshold MAC (**Table S3**, Bonf.threshold.MAC.specific). The GWAS data was processed for
152 associations with all SNPs used to generate Manhattan and QQ-plots (R notebook for processing GWAS
153 data: https://rpubs.com/mjulkowska/GWAS-root-shoot-Arabidopsis-salt-250kSNPs). Additionally, we
154 prioritized the genetic loci where multiple SNPs were associated with individual traits, or multiple traits
155 were associated with one genetic locus. Our final selection yielded 14 associations with traits measured
156 under control conditions, while 9 and 23 associations were specific to traits measured under 75 and 125
157 mM NaCl, respectively (**Table S3**). The GWAS output files can be accessed at Zenodo Repository (GWAS
158 using 250 k SNPs: https://doi.org/10.5281/zenodo.7271751; GWAS using 4 M SNPs:
159 https://doi.org/10.5281/zenodo.7271741). For the most promising loci (**Table S4**), the sequence
160 information of 147 accessions belonging to the HapMap population was downloaded from the 1001
161 genomes project website (1001genomes.org) and aligned with ClustalO as described in (Julkowska et al.,
162 2016). More details on plotting the genome divergence in the loci of interest can be found at
163 https://www.protocols.io/view/plotdivergence-for-plotting-the-natural-variation-x54v98y84l3e/v1. The
164 input and output files of Plot Divergence analysis can be found in Zenodo repository
165 (https://doi.org/10.5281/zenodo.7278021).

166 **Haplotype analysis**

167 For the most promising candidate loci (**Table S4**), we have identified the gene open reading frames that
168 were located within the genome-wide linkage-disequilibrium (LD) of the associated SNPs. The LD was
169 expanded if multiple SNPs were identified within the region, and the region of interest was expanded
170 based on the number of coding genes within the LD window. The protein-coding genes were subsequently
171 used for haplotype analysis. All the SNPs located within the gene coding region were used to perform a
172 haplotype analysis. The detailed protocol used for haplotype analysis can be accessed at
173 https://www.protocols.io/view/haplotype-analysis-of-the-cds-in-arabidopsis-thali-5jyl86n8v2wp/v1. The
174 accessions were grouped into haplotype groups depending on the combination of SNPs within the
175 protein-coding region of the gene of interest. The haplotypes represented by less than 3 accessions were
176 excluded from further analysis. The phenotypes of individual haplotypes were explored for significant
177 differences using ANOVA. The results for all investigated haplotypes can be accessed at Zenodo Repository
178 (https://doi.org/10.5281/zenodo.7277703).

179 **Identification of SR3G orthologs and paralogs**

180 DUF247 domain-containing orthologs from *Arabidopsis thaliana* and eight other species were identified
181 by reciprocal best BLAST within CoGe ((Nelson et al., 2018);
182 https://genomevolution.org/coge/CoGeBlast.pl) using *SR3G* (At3g50160) nucleotide sequence as query
183 with an E-value cutoff of 1.00E-10). The gene ID, species, and gene names been used in this study are
184 listed in **Table S5**. Sequence homologs were further confirmed by multiple alignments of those hits within
185 each species using Geneious Prime. Sequences with missing or incomplete DUF247 domains were

removed, with the exception of the mis-annotated DUF427 homologs in *Camelina sativa* which contained an extraneous intron that, after removal, resulted in a set of intact DUF247 open reading frame containing genes.

Phylogenetic and positive selection analysis of SR3G orthologs

Identified orthologs were translated into amino acid, then aligned by MUSCLE. Alignments were carefully validated by manual correction. Briefly, diverged insertions were trimmed, shifted frames were adjusted, and conserved regions after translation were retained for phylogeny reconstruction. Phylogenetic reconstruction was performed using the RAxML (Stamatakis, 2014) plug-in within Geneious (Geneious Prime 2022.1.1) with the GAMMA-GTR nucleotide model, rapid bootstrapping with a parsimony search, and 100 bootstraps. The distribution of *SR3G* and other DUF247 orthologs, root lengths for each branch, were visualized by software Geneious Prime.

To characterize any potential positive selection that might exist along certain branches of the inferred phylogeny, including SR3G and its orthologs, we performed a branch-site model A test on branches leading to SR3G, and branches leading to the clade containing SR3G and its closet orthologs using PAML4.0 (Stamatakis, 2014; Yang, 2007) as performed previously (Beilstein et al., 2015; Nelson et al., 2014). Specific branches are denoted as ω0, ω1, ω2, ω3, and ω-rest (Table S6). In the null hypothesis (H_0): we assigned a substitution rate (ω = dN/dS) along with $0 < \omega < 1$ or ω = 1 to all branches (represented by H_0: ω0 = ω1 = ω2 = ω3 = ω-rest). The alternative hypotheses (HAs) here allow for differential selection to be applied to respective branch(es). Specifically, the five alternative hypotheses are listed here: H_1: ω -rest branches = ω0 = ω3 = ω1 ≠ ω2, H_2: ω -rest branches = ω0 = ω1 = ω2 ≠ ω3, H_3: ω -rest branches = ω0 ≠ ω1 ≠ ω2 ≠ ω3, H_4: ω -rest branches ≠ ω0 ≠ ω1 ≠ ω2 ≠ ω3, H_{sep}: each branch has its unique ω value. To test these hypotheses, we further validate or reject alternative hypotheses by conducting a Chi-square test based on likelihood scores (Ln-L score) derived from the respective branch-site model A tests (Chi-square test cutoff: $P < 0.05$).

Screening candidate genes identified through GWAS

The genes located within the selected loci (**Table S4**) were further inspected for their contributions to root development and root:shoot ratio under control and salt stress conditions. The T-DNA insertion lines (**Table S4**) were genotyped using primers listed in **Table S4**, to confirm the homozygous insertion of the T-DNA within the phenotype lines. All the mutant lines were used for seed propagation in the controlled growth chamber with 16/8h of light/dark period, at 22°C, 60% humidity and 200 µmole m^{-1} s^{-1} under long-day conditions. The seeds of plants identified as homozygous were subsequently used for the experiment on agar plates, as described before for the Genome-Wide Association Study. A detailed protocol for plate assays can be accessed at https://www.protocols.io/view/plate-assay-for-identification-of-salt-stress-indu-eq2lyd1mwlx9/v1. The plate images were analyzed for root system architecture using Smart Root (Lobet et al., 2011) and the root:shoot ratio using the tool described before for Genome-Wide Association Study. The analysis of the mutant lines was performed in R. The data was first curated for selecting possible outliers within a genotype and subsequently used to fit growth functions for root and shoot tissues using exponential functions.

Screening SR3G mutants within root:shoot locus

The following T-DNA lines (listed in **Table S4**) were used for SR3G (AT3G50160) as the main GWAS candidate: *sr3g-4* (SAIL_690_E12, glufosinate resistant) and *sr3g-5* (SAIL_608_C06, glufosinate resistant). All T-DNA insertion alleles were in the background of Col-0 accession. The position of T-DNA insertions

228 was verified using PCR (primers listed in **Table S4**). RNAi lines targeting the neighboring of the *SR3G* or a
229 combination of *SR3G* and its neighboring *DUF247* genes included CSHL#3 targeting DUF130, CSHL#4
230 targeting SR3G, CSHL#5 targeting DUF130 and DUF170, CSHL#6 targeting DUF130 and DUF140, CSHL#7
231 targeting DUF10 and DUF150, CSHL#8 targeting DUF140 and DUF190, CSHL#10 targeting DUF180,
232 CSHL#11 targeting DUF150 and DUF170, CSHL#12 targeting DUF130, DUF140, DUF170, DUF180, and
233 DUF190, CSHL#13 targeting DUF140 and DUF170, CSHL#15 targeting DUF140, DUF170, DUF180, and
234 DUF190, CSHL#16 targeting DUF130, SR3G, and DUF170, CSHL#18 targeting DUF150 and DUF190,
235 CSHL#19 targeting DUF130, DUF140, DUF150, SR3G, DUF170, DUF180, and DUF190, CSHL#20 targeting
236 DUF130 and SR3G, CSHL#21 targeting DUF130 and DUF150, and CSHL#22 targeting DUF150 and SR3G.
237 The RNAi lines were verified using RT-qPCR, with the primers listed in **Table S4**. The following T-DNA
238 insertion alleles (also listed in **Table S4**) were used to characterize the neighboring genes of the *SR3G*
239 (AT3G50160): 120.2 (SAIL_382_A09), 140.1 (SALK_044685), 140.2 (SALK_005466), 140.3 (SALK_122700),
240 150.1 (SALK_003824), 150.3 (SALK_071080), 170.1 (SALK_009186), 170.2 (SALK_112602), 170.3
241 (SALK_008710), 170.4 (SALK_145999), 170.5 (SALK_072937), 190.2 (SALK_137791), 200.1 (SALK_113759),
242 200.2 (SALK_093701), 200.3 (SALK_129634). The primers used for genotyping PCR are shown in **Table S4**.

243 **Screening WRKY75 mutant lines and generation of *wrky75/sr3g* double mutant**

244 The following T-DNA insertion alleles were used for *WRKY75* (AT5G13080): *wrky75-1* (SALK_004954,
245 kanamycin resistant) and *wrky75-3* (SALKseq_046273, kanamycin resistant). All T-DNA insertion alleles
246 were in the background of Col-0 accession. The primers used for genotyping PCR are shown in **Table S4**.
247 Two sets of double mutant combinations were generated for *wrky75-3/sr3g-5*, with *wrky75-3* serving as
248 the maternal parent in one (referred to as line d) and *sr3g-5* serving as the maternal parent in the other
249 (referred to as line e).
250

251 **Plasmid construction and plant transformation**

252

253 For plant expression, all clones were constructed using the GreenGate cloning system (Lampropoulos et
254 al., 2013). We have generated full-length SR3G constructs, as well as three fragments - fragment A (from
255 amino acid number 1 to 216), fragment B (from amino acid number 217 to 468) and fragment C (from
256 amino acid number 469 to 503). Fragments A, B, AB, and ABC (full length) were cloned into entry vector
257 pGGC (GreenGate) with mVenus as N-terminal tag. SR3G fragments were PCR amplified using high-fidelity
258 DNA polymerase, and cloned as full-length cDNA or truncated version. The entry clone was evaluated
259 using Sanger sequencing to verify the absence of mutations. Promoters used included Ubiquitin 10
260 promoter (Norris et al., 1993). The list of constructs generated within this project can be found in **Table**
261 **S7.** The SR3G constructs generated in this paper and their corresponding vector maps can be accessed in
262 Zenodo repository
263 (https://zenodo.org/records/10788996?token=eyJhbGciOiJIUzUxMiJ9.eyJpZCI6IjI2ZjkzZGRlLTQ3M2YtND
264 BmZS04MmM5LTNhMjQ5MGFmOWY0NiIsImRhdGEiOnt9LCJyYW5kb20iOiI3OGNmY2UwM2YyMGFkNW
265 YwYjM2ZjAwOWYyM2VjNDNiNCJ9.NRWsSWHBe4srG720PncdfFjeDXQ0dATuI2BjSnca5sD1P_GAW5vhD_
266 bxOSBIH2f8txZObh5YRWH4Hkva0pzqXQ). The final constructs were validated via vector digestion, using
267 BaeGI for the constructs with fragments A, B, and AB and PvuI for the full length SR3G construct.
268 Subsequently, we transformed them into *Agrobacterium tumerfaciens* strain *GV3101*. Plant
269 transformations were conducted using the floral dip method (Clough and Bent, 1998). Transgenic plants
270 were selected for BASTA resistance (10 mg/L) for three generations, to ensure the homozygous and non-
271 segregating population of seedlings for each construct.

272 **Agar-based plate experiments for mutant lines**

273 Arabidopsis seeds were sterilized for 10 min with 50% bleach and rinsed five times using milli-Q water,
274 and germinated on ½ strength Murashige and Skoog (MS) medium containing 0.5% (w/v) sucrose, 0.1%
275 (w/v) 4-morpholineethanesulfonic acid (MES), and 1% (w/v) agar, with PH adjusted to 5.8 with KOH. After
276 24 h of vernalization at 4°C in the dark, the plates were placed in the Conviron growth chamber with the
277 light intensity of 130–150 µmol x m^{-2} x s^{-1} in a 16 h light / 8 h dark cycle at 21°C and 60% humidity. For
278 plate assays, 4 days after germination, the seedlings were transferred to ½ MS media supplemented with
279 0, 75, or 125 mM NaCl as indicated. The plates were scanned using EPSON scanner every other day,
280 starting from 4 days after germination until the plants were 14 days old. To analyze root system
281 architectural traits from the scanned plate images, we used SmartRoot plugin (Lobet et al., 2011) in ImageJ
282 to trace the root, and extracted root-related features in the CSV format followed by data analysis in R
283 (https://rpubs.com/mri23/913282)

284 **Evaluation of plant performance under salt stress in soil**

285 The seeds were germinated in ½ MS media for one week, as described for the agar-based plate
286 experiments. One week after germination, the seedlings were transplanted to the pot (12 x 4 cm insert)
287 containing the Cornell Mix soil (per batch combine: 0.16 m^3 of peat moss, 20.84 kg of vermiculite, 0.59 kg
288 of Uni-Mix fertilizer, and 2.27 kg of lime) watered to 100% water holding capacity and placed in the walk-
289 in growth chamber with the 16 h light / 8 h dark period, 22°C and 60% relative humidity throughout the
290 growth period. When all of the pots dried down to the weight corresponding to 50% of their water holding
291 capacity, they were soaked for 1 h in tap water or a 200 mM NaCl solution, resulting in an effective
292 concentration of 100 mM NaCl based on the 50% soil water holding capacity, which corresponded to a
293 moderate level of salt stress (Awlia et al., 2016). The control pots were soaked for the same length of time
294 in 0 mM NaCl solution, to account for the soil saturation effect. We then allowed the pots to be drained
295 for 2-3 h to eliminate excess moisture. The pots were placed under phenotyping rigs equipped with an
296 automated imaging system (Yu et al., 2023) and the pot weight was measured daily to maintain the
297 reference weight corresponding to 50% of the soil water holding capacity throughout the experiment. We
298 would like to note that this gravimetric based method for application of salt stress has been developed
299 for soils typically used for pot-grown plants, with relatively high water holding capacity (Awlia et al., 2016).
300 Within these specific conditions, no drought stress symptoms were observed.
301 To evaluate the growth of soil-grown plants, we used an in-house developed automated imaging
302 system using Raspberry Pi cameras to capture the growth dynamics over the period of two weeks (Yu et
303 al., 2023). The collected images were processed using the PlantCV pipeline (Gehan et al., 2017), followed
304 by the data analysis in R, as described here (https://rpubs.com/mjulkowska/sr3g_Maryam2021OctNov).

305 **Transient expression of SR3G constructs in tobacco epidermal leaf**

306 *Agrobacterium tumefaciens* strain *GV3101* containing cellular marker free GFP (*35S::GFP* with rifampicin
307 and spectinomycin resistant), generously provided by Professor Maria Harrison Lab at Boyce Thompson
308 Institute, or mVenus-SR3G constructs (including *UBQ10::mVenus-SR3G-full length*, *UBQ10::mVenus-*
309 *SR3G-fragment A*, *UBQ10::mVenus-SR3G-fragment B*, and *UBQ10::mVenus-SR3G-fragment AB*, all with
310 spectinomycin and tetracycline resistant) were grown in liquid YEP medium with appropriate antibiotics
311 overnight at 28°C while shaking. The following concentrations were used for antibiotics when used for
312 transient transformation: spectinomycin (50 ug/ml), tetracycline (10 ug/ml), and rifampicin (12.5 ug/ml).
313 Rifampicin and kanamycin (50 ug/ml) were used for P19 plasmid (generously provided by Maria Harrison
314 Lab at BTI) as a silencing inhibitor. The following day, OD_{600} was measured to be 0.3-0.5. The cultures were
315 then centrifuged at 8000x g for 2 min. The Agrobacterium pellet was resuspended in an induction buffer

316 containing 10 mM $MgCl_2$, 10 mM MES, pH 5.6, and supplemented with 200 µM acetosyringone and was
317 incubated for 2–4 h in the dark at room temperature. Leaves of 4-weeks-old *Nicotiana*
318 *benthamiana* plants were infiltrated using a syringe. After 48 hours, the fluorescence was visualized in
319 epidermal cells of leaf discs using confocal microscopy.
320 Confocal microscopy images were taken using the Leica TCS SP5 Laser Scanning Confocal
321 Microscope with the following setting: Excitation at wavelengths of 488 nm (GFP), 514 nm (mVenus), and
322 561 nm (chlorophyll autofluorescence) were provided using an argon or DPSS (Diode-Pumped Solid State)
323 laser. A spectral emission range of 505–525 nm for GFP, 526–560 nm for mVenus, and 680–700 nm for
324 chlorophyll autofluorescence was used.

325 **Elemental analysis**

326 The elemental analysis was performed using Inductively Coupled Plasma Atomic Emission Spectroscopy
327 (ICP-AES). For analysis of Na^+ and K^+ ions in roots and shoots of plate-grown seedlings, the plants were
328 grown on ½ x MS plates as described above. After two weeks of exposure to 0, 75 or 125 mM NaCl, root
329 and shoot tissues were harvested and measured for fresh weight, rinsed in milli-Q water and collected
330 into separate paper bags that were dried at 60 ˚C for 2-3 days. Subsequently, the dry weight was recorded.
331 Samples were digested in double distilled HNO3, followed by the addition of 60/40 nitric/perchloric acid
332 continuing incubation at 150 °C. Samples were processed for ICP-AES analysis using a Thermo iCap 7000
333 ICP-AES after diluted to 10 ml with deionized water. For soil-grown plants, the entire rosette leaves were
334 harvested at the end of week four and underwent a similar procedure as described above. Ion content
335 was calculated per dry weight for each sample, followed by data analysis in R
336 (sr3g:https://rpubs.com/mri23/913285, wrky75/sr3g double mutants:
337 https://rpubs.com/mri23/1157092 for plate-grown and sr3g:https://rpubs.com/mri23/913299 for soil-
338 grown seedlings).

339 **Electrolyte leakage analysis**

340 The electrolyte leakage measurement was done as previously described (Hu et al., 2015) with slight
341 modifications. In brief, for each plant, three leaf discs were incubated in 2 ml of distilled water for 24 h at
342 the light at room temperature with gentle shaking, followed by measuring the initial electrolyte leakage
343 using a conductivity meter (Horiba LAQUAtwin EC-11 Compact Conductivity Meter, # 3999960125). The
344 samples were then subjected to 80 ˚C for 2 h to release the total electrolyte, and cooled at room
345 temperature for 24 h. Final electrolyte leakage was measured the following day. The electrolyte leakage
346 percentage was calculated by dividing initial conductivity by final conductivity * 100 and followed by data
347 analysis in R (https://rpubs.com/mri23/913288 and https://rpubs.com/mri23/1102053).

348 **RT-qPCR analysis**

349 Total RNA was isolated from Arabidopsis seedlings root and shoot treated with or without 75 or 125 mM
350 NaCl for one week using the RNeasy Plant Mini Kit (Qiagen). RNA samples were cleaned at least twice
351 using RNase-free DNase (Qiagen) to remove genomic DNA contamination. One microgram of total RNA
352 was used for a reverse transcriptase reaction using iScript cDNA Synthesis Kit (Catalog #170-8891; Bio-
353 Rad). RT-qPCR analysis was conducted using iQ SYBRGreen Supermix (Bio-Rad) according to
354 manufacturer's instructions in the CFX96 real-time PCR system (Bio-Rad). *AT4G04120*
355 (*transposable_element_gene*) was used as a housekeeping gene for data normalization. RT-qPCR
356 experiments were conducted using three independent experiments, each with at least three biological
357 replicates. The list of primers used is shown in **Table S4**.

358 **Suberin staining**

359 Suberin content was examined in 6-days-old Arabidopsis roots treated with or without 75 mM NaCl for
360 two days using Fluorol Yellow 088 (FY; Santa Cruz Biotechnology Incorporation) staining. Seedlings grown
361 on agar plates (as described above for mutant screens) were incubated in a freshly prepared solution of
362 FY (0.01% [w/v] in lactic acid 85% [W/W]) at 70°C for 30 min, rinsed in milli-Q water for three times with
363 5 min each, and mounted on slides with 50% glycerol before confocal microscopy examination using
364 excitation at wavelength of 488 nm and a spectral emission range of 500–550 nm. Suberin quantification
365 was performed using the ImageJ software followed by data analysis in R
366 (https://rpubs.com/mri23/935019).

367 **Suberin monomer quantification using Gas Chromatography–Mass Spectrometry (GC-MS)**

368 100 - 150 Arabidopsis seedlings were grown on the plates for four complete days, transferred to 75 mM
369 salt plate for two days, and roots were harvested in distilled water to remove any remaining agar. Each
370 plate was treated as one biological replicate, and five plates were used for each genotype/condition. Each
371 plate of roots was collected into a microcentrifuge tube and dried in a speed vacuum concentrator
372 (Thermo Electron, Waltham, MA), and weighed. Approximately 1 mg of dried root were collected from
373 each plate. Suberin monomer quantification was performed according to (Delude et al., 2017; Kreszies et
374 al., 2019) with modifications. Dried root tissue was incubated in 1% cellulase plus 1% pectinase in 10 mM
375 citrate buffer (pH 3.0) for two weeks, with the incubation solution changed every three days. After the
376 cellulase/pectinase solution was removed, chloroform/methanol solution (2:1 and 1:2, v/v) were mixed
377 with the root tissue for three days respectively, to remove lipids. The remaining root tissue was mixed
378 with 1 ml freshly prepared 5% H_2SO_4 in methanol (v/v) and 200 µl of toluene containing 20 µg of
379 heptadecanoic acid as internal standard, sealed in an 8 ml capped tube and heated at 85°C for 90 min.
380 After samples were cooled to room temperature, 200 µl hexane and 1.5 ml 0.9% sodium chloride in water
381 are added to the capped tube with shaking. After centrifuging at 1000 *g* for 1 min, the upper organic phase
382 was transferred to a glass insert of GC vial and dried. 40 µl pyridine was added to the glass insert, 40 µl
383 *N,O*-bis(trimethylsilyl)trifluoroacetamide (Restek, Bellefonte, PA) was added subsequently, incubated at
384 65°C for 2 h. Standards of 1 µl derivatized sample was injected into GCMS (Agilent 6890-5975, Santa Clara,
385 CA), with the inlet temperature of 250°C, column helium flow of 1 ml/min, and a split ratio of 5:1. The
386 oven temperature was held at 50°C for 1 min, raised to 200°C at the rate of 25°C/min, held at 200°C for 1
387 min, raised to 320°C at the rate of 10°C/min, and finally held at 320°C for 5 min. 1-Docosanol (22:0-OH),
388 1-eicosanol (20:0-OH), hexadecanedioic acid (16:0-DCA), 1-hexadecanol (16:0-OH), 16-hydroxy
389 hexadecanoic acid (16:0-ωOH), C4 - C24 Even Carbon Saturated FAMEs (Sigma 49453-U), 20-hydroxy
390 arachidic acid (20:0-ωOH) (Cayman Chemical Company, Ann Arbor, Michigan) standards were input at 2.5
391 µg, 5 µg, 10 µg, and 20 µg into a mixture and processed with the same procedure as the tested samples
392 to build the standard curve. The MS spectrum of derivatized products with ±2n carbon number of these
393 standards was calculated and identified, referring tom the retention order in (Delude et al., 2017).

394 **Yeast One-hybrid Assay**

395 The respective combinations of *pB42AD*-fusion effectors and *pLacZ* reporters were co-transformed to
396 yeast strain EGY48 (Shanghai Maokang, China). Transformants were selected and grown on SD/-Trp-Ura
397 medium. The putative interactions were observed on SD/-Trp/-Ura + X-Gal after a 3d-incubation at 30°C.
398 Yeast transformation and growth assay were performed as described in the Yeast Protocols Handbook
399 (BD Clontech, USA). In brief, 631 bp of the *DUF247-150* (AT3G50150) and 953 bp of the *SR3G* (At3g50160)
400 promoter region were separately ligated into *pLacZ* vector as the reporter, while the CDS of *WRKY75*
401 (AT5G13080) was cloned into *pB42AD* vector as the effector. The *SR3G::pLacZ* and *WRKY75-pB42AD* were

402 transformed into the yeast strain EGY48(Shanghai Maokang, China). The respective combinations of
403 *pB42AD*-fusion effectors and *pLacZ* reporters were co-transformed into yeast strain EGY48.
404 Transformants were selected and grown on SD/-Trp-Ura medium. The putative interactions were
405 observed on SD/-Trp/-Ura + X-Gal after a 3d-incubation at 30°C. Yeast transformation and liquid assay
406 were conducted as described in the Yeast Protocols Handbook (BD Clontech, USA). The primers used for
407 the Y1H assay are shown in **Table S4.**

408 # Results

409 ## Natural variation in salt stress-induced changes in root:shoot ratio

410 To investigate salt stress-induced changes in root:shoot ratio, we developed a custom tool that quantifies
411 green and white pixels, corresponding to shoot and root of Arabidopsis seedlings grown on agar plates
412 (**Fig. 1**). The projected area of root and shoot showed high correlation with root and shoot fresh weight
413 (**Fig. S1**), indicating that projected root and shoot area can be used as an accurate proxy to non-
414 destructively measure the increase in root and shoot biomass from the images of seedlings grown on agar
415 plates.

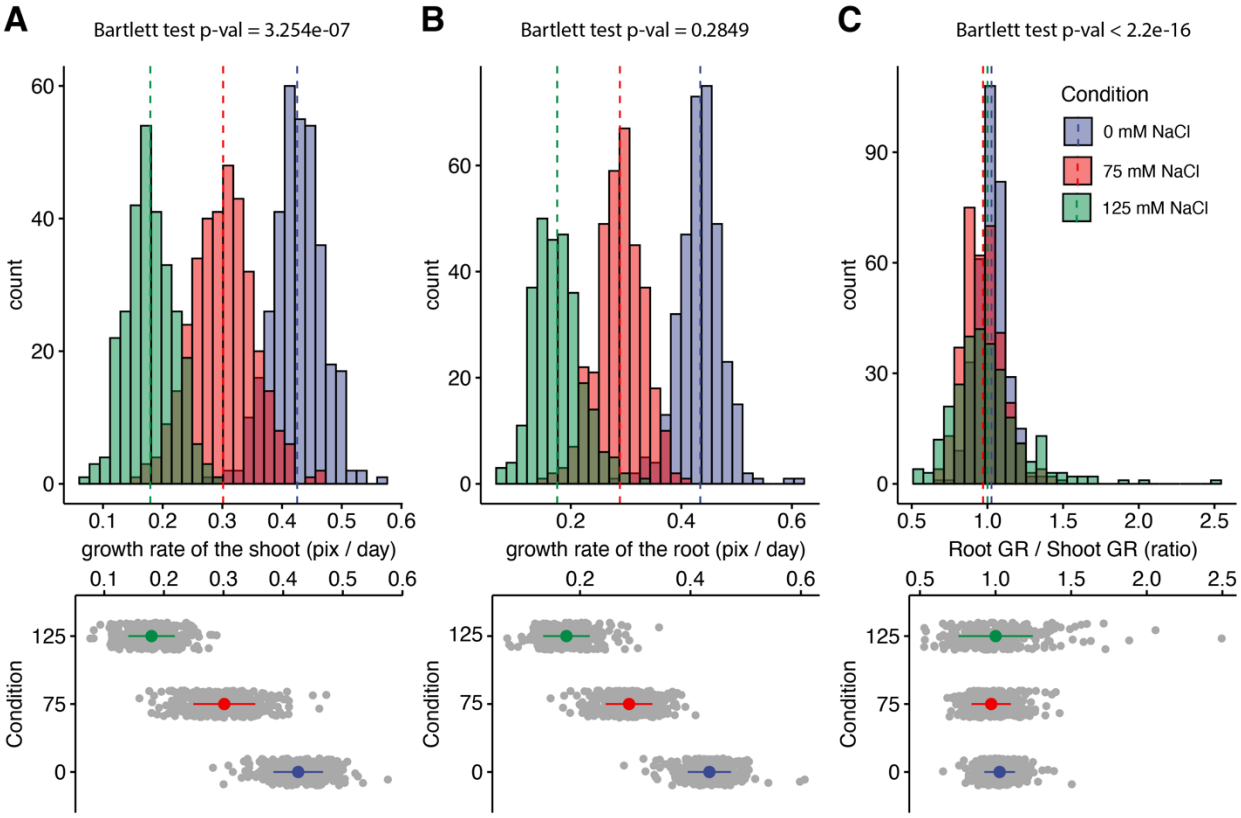

Figure 1. Salt stress is causing discoordination of root and shoot growth. Arabidopsis HapMap population was screened for salt stress-induced changes in root:shoot ratio. The increase in the projected area of shoot and root (Fig. S2) was used to estimate **(A)** shoot and **(B)** root exponential growth rate. **(C)** The root:shoot growth rate ratio was calculated per genotype. The histograms represent the number of accessions across three studied conditions (0, 75 and 125 mM NaCl), whereas the population average is indicated using the dashed line. Additionally, the distribution of the genotypes within each treatment was visualized using the error plots (lower panel), where population average and standard error is indicated using a colored point and a line, respectively. Individual grey points represent individual genotypes.

416
417 Using our custom tool, we re-analyzed the data consisting of 360 Arabidopsis accessions grown
418 on plates supplemented with 0, 75, and 125 mM NaCl (Julkowska et al., 2017), for salt stress-induced
419 changes in the root:shoot ratio (**Fig. 1, Fig. S2**). The growth of root and shoot for each plant was estimated
420 using the exponential function. Salt stress-induced reduction in growth rate was observed to be dose-
421 dependent for both root and shoot (**Fig. 1A-B**). In general, the root growth was more sensitive to salt
422 stress compared to shoot growth, with the population-wide relative growth rates reduced to a fraction of
423 0.67 and 0.41 of the growth rates observed at control for 75 and 125 mM NaCl, respectively. In
424 comparison, the growth rates of the shoot were significantly reduced to 0.71 and 0.43 of the control in 75

425 and 125 mM NaCl treatments, respectively (**Fig. S3**). While the mean value of root:shoot growth rate did
426 not change upon salt stress treatment, the variance in the root:shoot ratio significantly expanded with
427 the increasing concentrations of salt (**Fig. 1C**). These results suggest that while root and shoot growth are
428 well coordinated under non-stress conditions, salt stress exposure results in loss of coordination of organ
429 growth across Arabidopsis accessions. To test whether there is a clear directional correlation between the
430 change in root:shoot ratio and overall salt stress tolerance, we have used the overall seedling size as a
431 proxy for plant salt tolerance (**Fig. S4, S5**). No significant correlation was found between the root:shoot
432 growth ratio and total seedling size (**Fig. S4, S5**), indicating that the relationship between coordination of
433 root and shoot growth and salt tolerance during the early seedling establishment is complex.

434 **Identification of genetic components underlying salt-induced changes in root:shoot ratio**

435 To identify genetic components underlying salt-induced changes in root:shoot ratio, we used the collected
436 data as an input for GWAS. The associations were evaluated based on the p-value, the number of SNPs
437 within the locus, and the number of traits associated with individual loci. As Bonferroni threshold differs
438 depending on the minor allele count (MAC) considered, we identified significant associations based on a
439 Bonferroni threshold for each subpopulation of SNPs based on MAC (**Table S3**). While we conducted a
440 GWAS on directly measured traits, as well as their Salt Tolerance Index (STI) values, however the amount
441 of associations with STI was much lower compared to directly measured traits (**Table S3**). This observation
442 aligns with the understanding that plastic responses to environmental conditions tend to be genetically
443 more complex. This complexity likely stems from the involvement of more genetic regulators compared
444 to low-plasticity phenotypes.
445 The initial GWAS was performed using 250 k SNPs (Horton et al., 2012), and led to the
446 identification of 14 significantly associated loci, of which 3 and 7 loci were associated with traits measured
447 at 75 or 125 mM NaCl treatments, respectively. We identified one salt specific association on chromosome
448 2 (**Fig. S6**), where two SNPs were identified within AT2G27300 encoding NAC-domain containing
449 transcription factor (NTL8). Additionally, salt-induced changes in root:shoot ratio and shoot:total seedling
450 area were associated with SNPs on chromosome 3, where 2 significantly associated SNPs were flanking
451 AT3G22430, encoding an unknown gene encoding a domain of unknown function (**Fig. S7**).
452 To refine our analysis and further prioritize candidate genes for validation, we repeated the GWAS
453 using a higher-density 4M SNP panel (1001 Genomes Consortium, 2016). This increased SNP density
454 provided more associations and highlighted loci with greater confidence due to the higher resolution. The
455 higher-density panel also allowed us to capture different linkage disequilibrium (LD) blocks across the
456 genome. One locus on chromosome 2, detected by both the 250K and 4M SNP panels, appeared to be in
457 a region of strong LD or possibly under selection, consistently identified by both panels. However, most
458 loci were not detected by the lower-density 250K panel, likely due to differences in the panels' resolution
459 and statistical power.
460 The new GWAS with the 4M SNP panel revealed 32 additional loci, with only one locus (locus 30,
461 **Table S3**). being detected by both the 250K and 4M SNP panels. We prioritized the identified loci based
462 on several factors, including the number of significantly associated SNPs, MAC, and the number of traits
463 associated with each locus. This led to the identification of three loci of major interest (**Table S4**). We
464 further examined the regions in LD with the significantly associated SNPs for sequence divergence and
465 open reading frames (**Fig. 2, Fig. S8, Fig. S9**).
466 Out of identified associations, locus 30 stood out as it consisted of nine SNPs associated with p-
467 value above the Bonferroni threshold, and was associated with both root:shoot and shoot:total seedling
468 area at 6 and 8 days after transfer of the seedling to 125 mM NaCl (**Fig. 2A-B, Fig. S8, Table S4**). The
469 significantly associated SNPs were located in and around the gene coding region of AT3G50160, which
470 encodes a domain of unknown function 247 (DUF247). We investigated the region for sequence
471 divergence, and found that the region contained not only a high degree of sequence diversity but also

472 potential structural variants (**Fig. 2C**). To identify allelic variation underlying the initial associations, we
473 performed haplotype analysis, where accessions with shared SNP pattern within the protein-coding part
474 of AT3G50160 were grouped into individual haplotype-groups (**Fig. 2D**). Each unique haplotype,
475 represented by at least three accessions, was subsequently studied for differences in observed
476 phenotypes. We observed that Haplotype 1, represented by 46 accessions including Col-0, was
477 significantly different from Haplotype 11, represented by 11 accessions including Blh-1, in shoot-per-total
478 seedling area at 6 days after transfer to 125 mM NaCl (**Fig. 2D**), as well as shoot growth rate and relative
479 shoot growth rate at 125 mM NaCl (**Fig. S9**). Upon further investigation and sequencing of AT3G50160 in
480 both Col-0 and Blh-1 accessions, we discovered that the Blh-1 allele carries a large insertion at 644
481 nucleotides downstream from the ATG of AT3G50160, followed by multiple other sequence variations
482 (**Fig. S10**). The first insertion leads to a premature STOP-codon within the DUF247 domain after Gly-215
483 (**Fig. 2E, Fig. S11**), resulting in a truncated protein that still carries a nuclear localization signal and coiled-
484 coil domain, but is missing a major part of the calcium-binding domain and a predicted transmembrane
485 domain (**Fig. S12**). As there are other DUF247s within the locus associated with salt-induced changes in
486 root:shoot ratio, we decided to name the gene containing majority of the associated SNPs (At3g50160) as

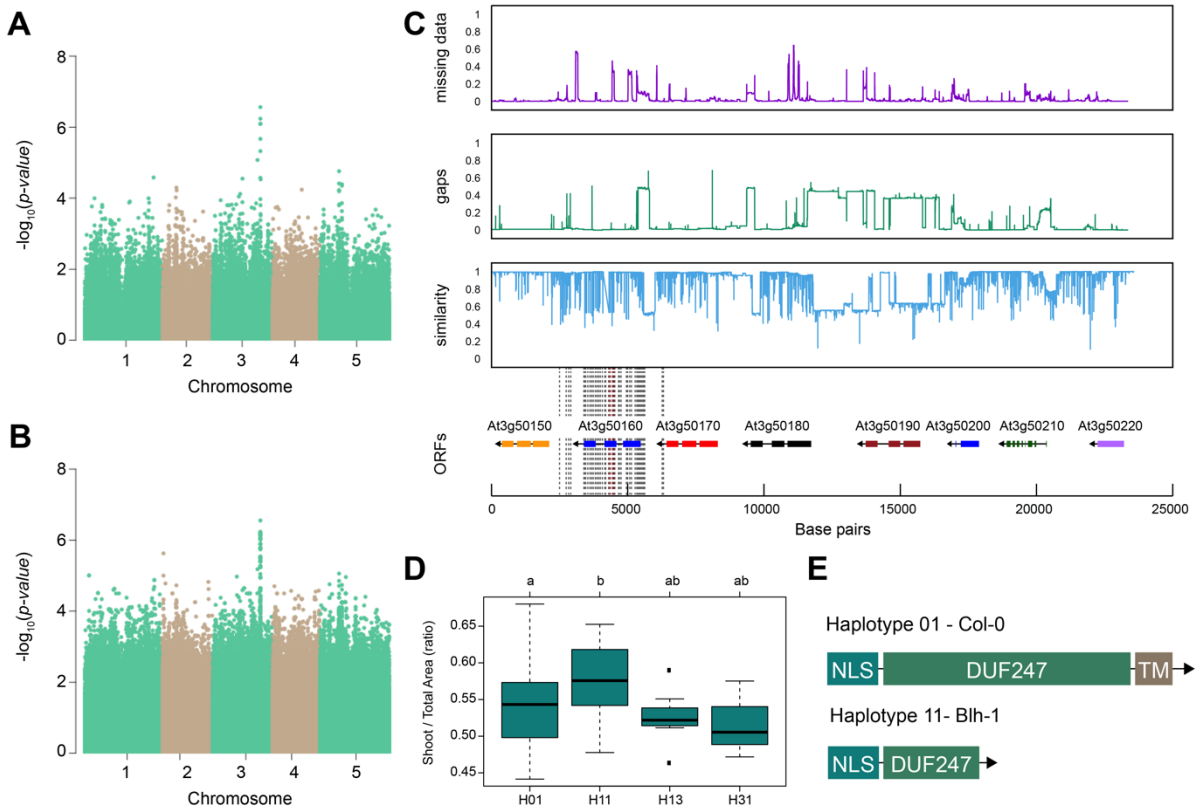

Figure 2. SR3G is associated with salt stress-induced changes in shoot-per-total seedling area ratio. The salt induced changes in root-to-shoot and shoot-per-total seedling area ratios were used as an input for GWAS. Manhattan plots representing the associations of shoot-per-total seedling area recorded 6 days after transfer to 125 mM NaCl and **(A)** 250 k SNPs and **(B)** 4 M SNPs. **(C)** Significant associations were found with the SNPs forming a locus on chromosome 3 in and around SR3G (AT3G50160), encoding Domain of Unknown Function 247 (DUF247). The natural variation in the LD region was studied in 162 accessions sequenced by 1001 Genomes Project. The upper panel represents portion of the missing data, upper middle panel represents deletions relative to Col-0, while lower middle panel represents the sequence similarity compared to Col-0. The bottom panel represents the open reading frames (ORFs) within the LD, and the location of associated SNPs is indicated with the dashed lines. Red dashed lines represent associations above Bonferroni threshold in 250k SNP mapping, while grey lines represent associations with -log10(p-value) > 5 in the 4M SNP mapping. **(D)** The haplotype analysis performed using SNPs located within the coding region of the SR3G revealed significant differences in shoot-per-total seedling area recorded 6 days after transfer to 125 mM NaCl between Haplotype groups 1 (represented by 46 accessions, including Col-0) and 11 (represented by 11 accessions, including Blh-1). The significant differences between individual haplotype groups were tested using ANOVA with Tukey HSD to identify significantly different groups. **(E)** Upon further sequencing of SR3G in accessions from Haplotype 1 and 11, revealed two 200 bp insertions within SR3G exons in 4 tested accessions belonging to haplotype 11 group. These 200 bp insertions resulted in a premature STOP-codon within the DUF247 domain (after Gly-215).

487 Salt Root:shoot Ratio Regulator Gene (SR3G). Together, these results suggest that the allelic variation in
488 SR3G protein sequence might underlie the observed differences in root:shoot ratio under salt stress
489 conditions.

490 **Evolutionary context of SR3G locus reveals its origin in local genome duplication**

491 SR3G sits in what appears to be a tandemly duplicated array of DUF247s along Arabidopsis chromosome
492 3. The genome-wide identification of SR3G included eight DUF247 paralogs, AT3G50120, AT3G50130,
493 AT3G50140, AT3G50150, AT3G50170, AT3G50180, AT3G50190, and AT3G50200. Reciprocal best BLAST
494 within CoGe's BLAST tool of these nine DUF247 paralogs against the genomes of seven other Brassicaceae
495 (see **Table S5**) revealed a total of 50 potential orthologs used for downstream analysis. While the copy
496 number of DUF247 loci are similar across the examined species, the noted exceptions are those with
497 recent whole genome duplication events (*Brassica rapa* and *Camelina sativa*). Given these data, it appears
498 that DUF247 loci are commonly tandemly duplicated, although the eight paralogs observed in Arabidopsis
499 represents an extreme case for this gene family.
500 To examine conservation within the predicted DUF247 functional domains, we generated an
501 amino-acid based multiple sequence alignment using MUSCLE. All of the identified DUF247 proteins
502 contained the DUF247 domain near the center of the translated sequence. While partial deletions were
503 identified outside of the DUF247 domain at the C-terminus of a few DUF247s, such as *CARHR159180*,
504 *Csa09g052970*, and *Bra01902*, in general the DUF247 domains were highly conserved across Brassicaceae.
505 The amino acid sequences spanning the "coiled-coil domain" (Amino acid position: Met153-Lys173),
506 putative Ca^{2+} binding domain (Amino acid position: Gly210-Phe372), and super polar fragment (Amino
507 acid position: Ser301-Ile320) were further selected for phylogenetic reconstruction (**Fig. 3B**). The resulting
508 phylogeny demonstrated that SR3G is sister to a clade containing AT3G50150 and representatives from
509 *C. sativa*, *Capsella rubella,* and *A. lyrata*, with representative DUF247s from *B. rapa* and
510 *Eutrema salsugineum* serving as a monophyletic outgroup. These data support a hypothesis where SR3G
511 is a recent duplicate (likely A/C Clade specific; Forsythe et al., 2020) of AT3G50150 and that representative
512 SR3G sequences in *C. sativa*, *C. rubella*, and *A. lyrata* have been lost.
513 Given the specific retention of AT3G50150 in *A. thaliana*, we next tested whether this locus is
514 experiencing directional selection. To test this assumption, we grouped the branches leading to SR3G into
515 four groups (**Figure 3B**: ω0, ω1, ω2, and ω-rest) and then performed a branch-site model A hypothesis
516 test**.** In our null hypothesis (H_0), we hypothesized that all branches have the same selection pressure (H_0:
517 ω -rest branches = ω0 = ω3 = ω1 = ω2; see **Table S6** for omega values for each hypothesis). For our
518 alternative hypothesis, we created five different ω groups to cover scenarios where specific branches may
519 be experiencing directional selection (See Methods). Based on our analysis, the branch leading to SR3G is
520 experiencing directional selection (likelihood score = 20625.5, Chi-square derived P value; P = 0.00418).
521 Interestingly, no other branches appeared to be experiencing the same selection. To pinpoint specific
522 amino acids within SR3G under selection, we performed the Bayes Empirical Bayes (BEB) test, identifying
523 three sites with a posterior probability > 0.90, including 124C (P = 0.992), 206A (P = 0.951), and 209A (P =
524 0.988). Two out of three sites are located at the putative Ca^{2+} binding site and all three sites possess a
525 unique amino acid compared with the other 49 amino acid sequences (**Fig. 3C**).

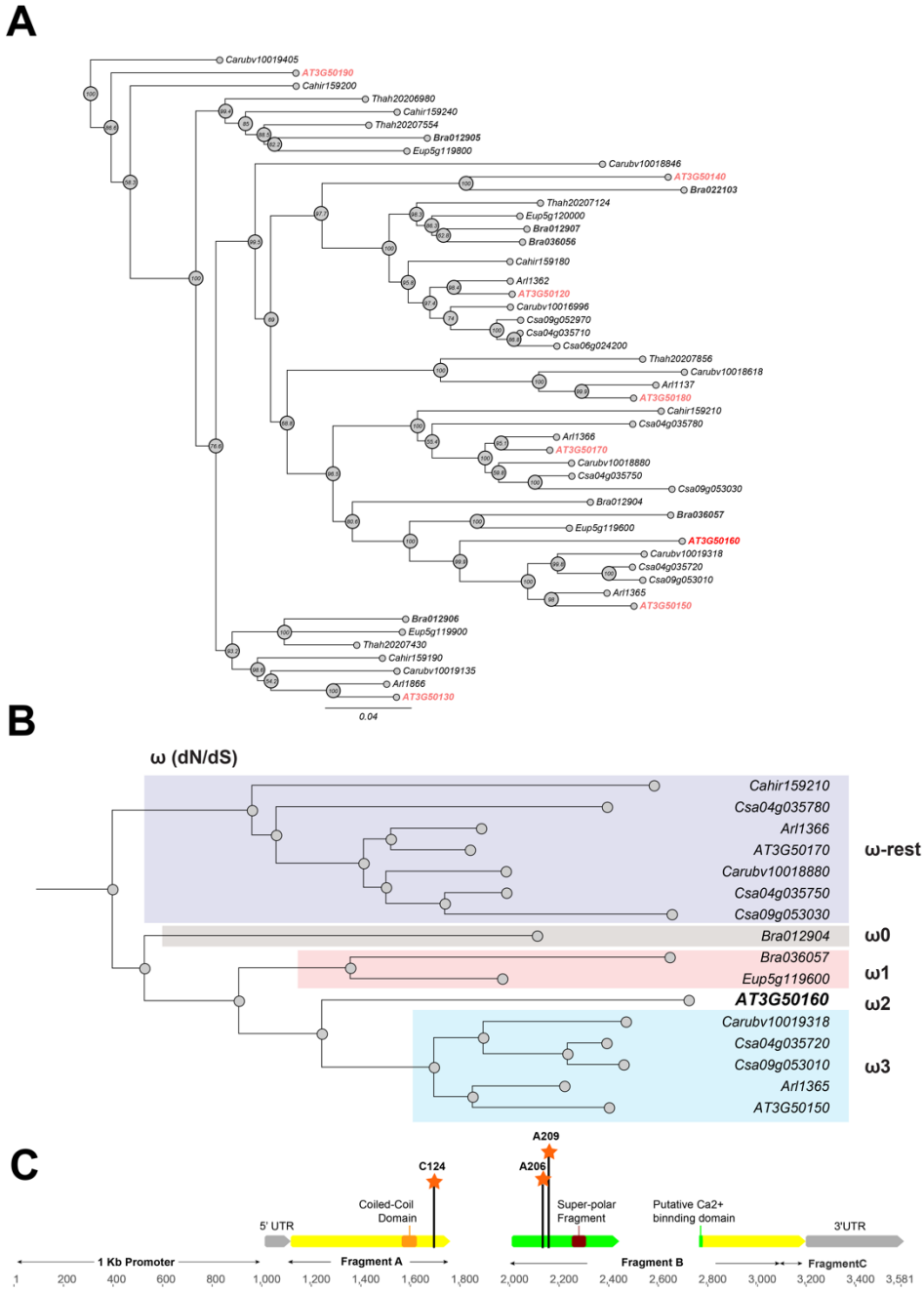

Figure 3. Phylogeny and positive selection analysis of SR3G and its orthologs from other species. The orthologous genes of SR3G (AT3G50160) from other seven species were identified using Go-GeBlast (E-value < 1.00E-10). **(A)** The protein sequences of the 50 homologous genes were aligned by MUSCLE and then an unrooted phylogenetic tree was reconstructed by a Maximum -likelihood (ML)-derived style by RAxML (Bootstrap number: 100). **(B)** A positive selection analysis was conducted by branch-site model A test: Specifically, we hypothesized the differential or constant dN/dS (ω) substitution rate among the closely distant branches leading to DUF247 (AT3G50160) (See Method & Materials for details). These branches were marked as ω1 (light brown branch), ω2 (DUF247-specific branch), ω3 (light blue branch), and ω-resvt (light purple branch). **(C)** The gene structure of DUF247 (AT3G50160) was illustrated by wide arrows (grey arrow: 5 and 3' UTR, yellow arrow: coding-region). The regions used for cloning (Fragment A, B, and C) were marked by narrow arrows along with "Coil-Coil Domain" and "Super-polar Fragment" marked on Fragment A and B, respectively. Lastly, the Bayes Empirical Bayes (BEB) was performed to test the probability of sites along with ω > 1 over the DUF247 (AT3G50160). Three sites were generated with a posterior probability > 0.90: 124C (P = 0.992), 206A (P = 0.951), and 209A (P = 0.988). These three sites were marked with an orange asterisk and assumed to have been undergoing positive selection.

526

527 ***SR3G* expression is enhanced in root by salt stress**

528 To identify the developmental window and specific plant tissues where the *SR3G* gene is active, we
529 examined its expression pattern. Based on Arabidopsis eFP Browser (http://bar.utoronto.ca/), *SR3G*
530 expression is relatively low, and restricted to the early stages of seedling development (**Fig. S13A**). Upon
531 examining the expression profiles specific to different tissues, we observed that *SR3G* is predominantly
532 expressed in the root stele (**Fig. S13B**). Moreover, *SR3G* expression was induced by salt stress (**Fig. S13C**).
533 To validate these results, we performed RT-qPCR on 11 days old seedlings of Col-0 exposed to 0 or 75 mM
534 NaCl for 7 days. In Col-0 seedlings, the transcript levels of *SR3G* were significantly higher in shoot

compared to the root tissue (**Fig. 4A**). Interestingly, the *SR3G* transcripts increased only in root upon salt stress exposure but not in shoot (**Fig. 4A**). These results suggest that *SR3G* is the most prominent DUF247 studied within our study to affect root development under salt stress.

We further examined expression profiles of other *DUF247* genes that directly neighbor *SR3G* in response to salt stress using the eFP Browser. We observed similar expression patterns as *SR3G* for other *DUF247s* including At3g50150, indicating their responsiveness to salt stress (**Fig. S14**). Because *DUF247-150* (At3g50150) is closely located to the *SR3G* in chromosome 3, we investigated its gene expression in young seedlings. We observed that its expression was significantly higher in shoot compared to the root tissue. However, its expression remained unchanged in both root and shoot under salt stress (**Fig. 4B**). For the remaining *DUF247* genes (At3g50120 and At3g50200), we observed no significant changes, while others (At3g50130, At3g50140, At3g50170, At3g50180) showed reduced expression upon exposure to salt stress (**Fig. S14**). These results suggest that *SR3G* is the most prominent DUF247 studied herein involve in regulation of root development under salt stress.

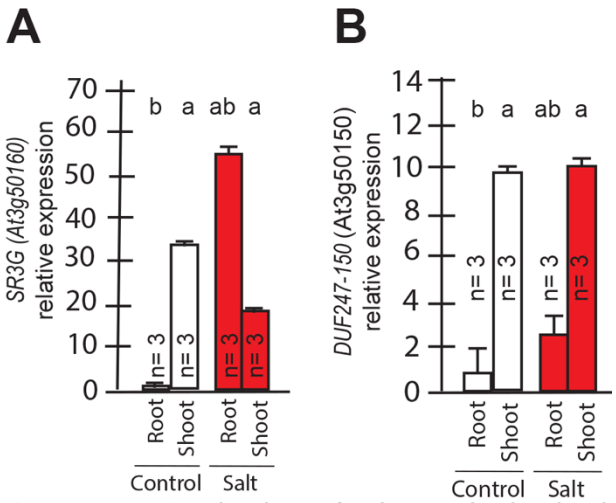

Figure 4. Transcript abundances for the two closely related DUF247s. Expression of **(A)** SR3G (AT3G50160) and **(B)** its closest homologue DUF247-150 (AT3G50150) were measured in Col-0 seedlings grown with and without salt stress. RT-qPCR analyses were conducted using seedlings grown on 1/2x MS for 4 d and then followed by transferring to the treatment plates with or without 75 mM NaCl for one week. Mean values are shown ± SE, with number of replicates (n) shown in each graph. AT4G04120 was used as a reference gene for normalization. Significance was determined by the Tukey–Kramer HSD test in JMP.

SR3G relocates from plasma membrane to nucleus/cytosol after removal of its transmembrane domain

SR3G protein is predicted to contain a nuclear localization signal (Lys15-Ala19), a coiled-coil domain (Met153-Lys173), a $Ca2^{+}$ binding pocket (Gly210-Phe372), and a trans-membrane domain (Pro469-Thr503) (**Fig. S15**). We generated constitutive expression constructs of full-length *SR3G* gene CDS, and a combination of individual domains (refer to as A, B, and AB domains) to identify their subcellular localization (**Fig. S15**). Fragment A comprised a nuclear localization signal, a coiled-coil domain, and the initial segment of the Ca^{2+} binding pocket, encompassing seven amino acids. Fragment B encompassed the remaining segment of the Ca^{2+} binding pocket. Fragment C only included the transmembrane domain. All constructs contained N-terminal fusion of mVenus. The individual constructs were used in transient expression assay in tobacco leaves. Our result showed that full-length SR3G localizes to the plasma membrane (**Fig. 5A**) as its signal overlapped with FM4-64, the plasma membrane marker (**Fig. 5B**). The SR3G fragments from which the transmembrane domain was excluded—namely fragments A, B, and AB—exhibited localization in both the nucleus and cytosol, resembling the pattern observed with free-GFP localization (**Fig. 5C-F**). It is noteworthy that while the signal from fragment A was directed to both the cytosol and nucleus, its intensity was notably stronger in the nucleus (**Fig. 5C**), aligning with the prediction that it contains the nuclear localization signal. Together, these findings indicate that the positioning of SR3G within the plasma membrane is due to the transmembrane domain encoded within the fragment C, and its removal could potentially release the protein into both the nucleus and cytosol.

579

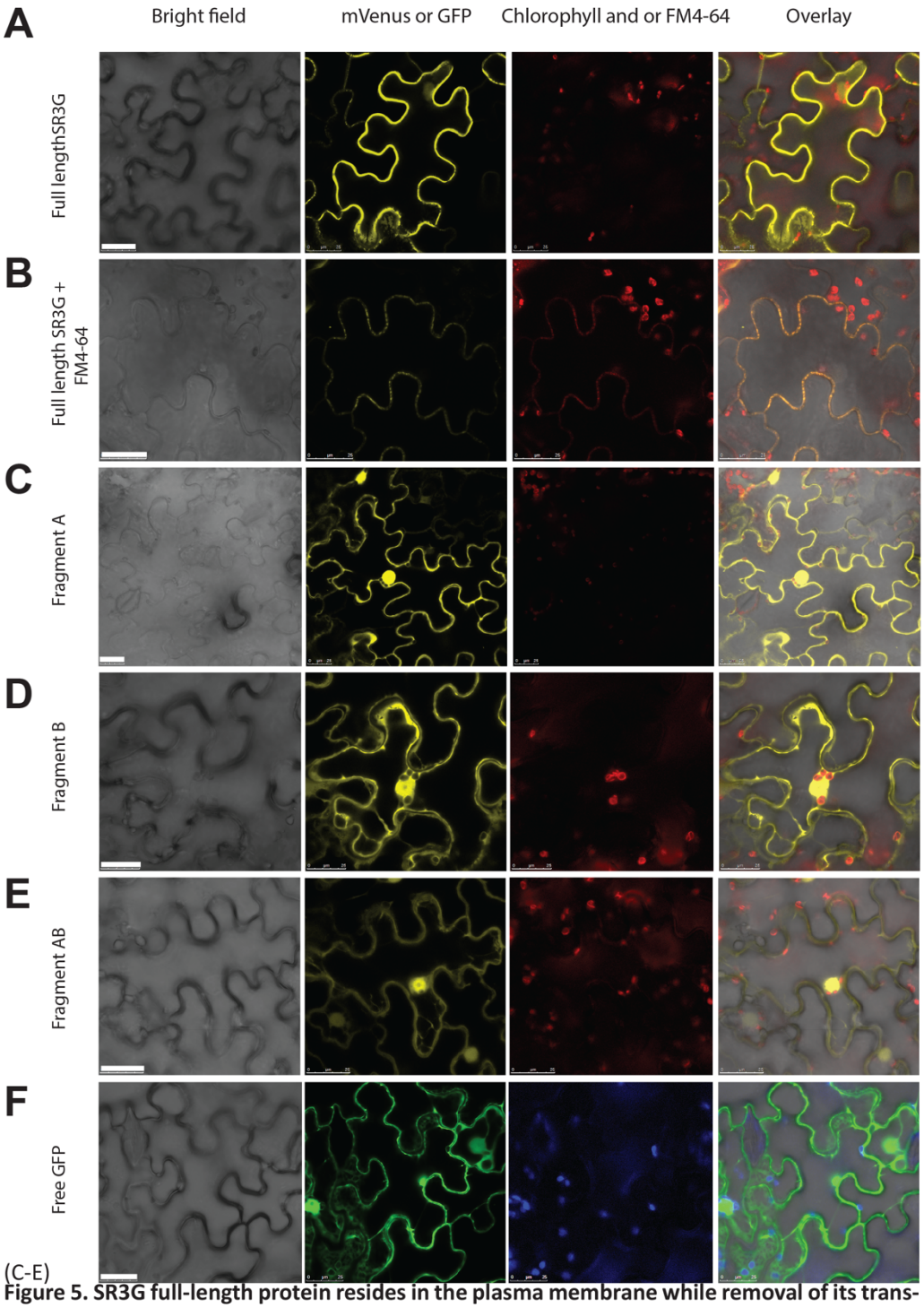

(C-E)

Figure 5. SR3G full-length protein resides in the plasma membrane while removal of its transmembrane domain results in protein relocation to nucleus and cytosol. (A-B) SR3G full-length protein or (C-E) truncated versions fused to mVenus at the N-terminus were agro-infiltrated into the Nicotiana benthamiana leaves for transient expression. Shown are a bright-field image of transfected leaf cells and mVenus-SR3G-mediated fluorescence as well as GFP-based subcellular marker. **(A)** Localization of full-length SR3G alone or **(B)** in combination with the known plasma membrane dye, FM4-64. Localization of truncated versions of SR3G are shown for **(C)** SR3G-Fragment A, **(D)** SR3G-Fragment B, and **(E)** SR3G-Fragment AB. **(F)** Free GFP was used as a nuclear and cytosolic marker. Scale bar = 25 µm.

580 **Lower expression of *SR3G* results in reduced lateral root development under salt stress**

581 To investigate role of *SR3G* in salt-induced changes in root growth and development, we studied the root
582 system architecture of two T-DNA insertion lines: *sr3g-4* (SAIL_690_E12) and *sr3g-5* (SAIL_608_C06)
583 localized in second exon and first intron region of the *SR3G* gene, respectively (**Fig. S16A**). Among these
584 two mutant lines, *SR3G* expression was reduced in the *sr3g-5* mutant compared to Col-0 (**Fig. S16B**),
585 indicating the *sr3g-5* is a knockdown mutant. We did not observe any differences in *SR3G* transcript
586 abundance between *sr3g-4* and Col-0 (**Fig. S16B**). Moreover, we examined the transcript abundance of
587 the closely related gene (i.e., *DUF247-150, At3g50150*) in the *sr3g-5* mutant, and found no significant
588 difference. In the case that *DUF247-150* would act redundantly to *SR3G*, we would expect that the
589 expression of *DUF247-150* would be increased in *SR3G* knockdown mutant. As this is not the case, these
590 results further contribute to the evidence that *SR3G* and *DUF247-150* are not acting redundantly (**Fig.**
591 **S16C**).

592 Two T-DNA insertion lines were subsequently studied for salt-induced alterations in root
593 architecture (**Fig. 6 and Fig. S17 and S18**). Among the various features of the root system architecture that
594 we investigated (**Fig. S17**), *sr3g-5* exhibited a significantly reduced growth rate of lateral roots under 75
595 mM NaCl, but not under 125 mM NaCl, when compared to Col-0 (**Fig. 6A**). Likewise, the *sr3g-5* mutant
596 displayed a significant reduction in the Stress Tolerance Index (STI), calculated as the ratio of growth rate
597 under salt to growth rate under control conditions, for lateral root length under 75 mM NaCl (**Fig. 6B**). No
598 significant difference was observed between *sr3g-4* and Col-0 (**Fig. S18**), except for Stress Tolerance Index
599 (STI) calculated using growth rates of lateral root length and number, consistent with the observations
600 made for the *sr3g-5* mutant line (**Fig. 6B).** Based on the RT-qPCR results (**Fig. S16**), we proceeded to further
601 investigate the role of *SR3G* in salt stress, focusing on the sr3g-5 mutant in our subsequent investigations.

602 As Na^+ exclusion from the shoot is one of the main mechanisms of salt tolerance (Julkowska et al.,
603 2017; Møller et al., 2009; Munns and Tester, 2008), we further investigated the role of *SR3G* in ion
604 exclusion using plate-grown seedlings. We used root and shoot samples collected for Col-0 and *sr3g-5*
605 mutant to examine Na^+ and K^+ accumulation using ICP-AES at 14 days after exposure to salt stress. We
606 observed no significant differences between Col-0 and *sr3g-5* mutant for Na^+ and K^+ accumulations and
607 their corresponding ratio upon salt stress exposure (**Fig. S17**, **Fig. 6C**). These results suggest that *SR3G*
608 plays a role in root development under the salt, but does not affect ion accumulation at early
609 developmental stages.

610 To evaluate the effects of other closely related DUF247 genes on root development, we have
611 investigated the T-DNA insertion lines targeting the neighboring DUF247 genes (AT3G50120, AT3G50130,
612 AT3G50140, AT3G50150, AT3G50170, AT3G50180, AT3G50190, AT3G50200), and RNAi lines targeting
613 one or more DUF247s within the interval (**Table S4, Fig. S19-S23**). For the screened T-DNA insertion lines
614 (**Fig. S19-20**), we have not observed consistent changes in main or lateral root development in either
615 control or salt stress conditions across alleles targeting the same gene. The only exception was *DUF247-*
616 *200* encoded by AT3G50200, where two out of three studied T-DNA insertion alleles exhibited increased
617 salt tolerance index for main root growth rate (**Fig. S20**).

618 For the screened RNAi lines (**Table S4, Fig. S21-S23**), we observed the most interesting root
619 architecture phenotypes in lines targeting the neighboring genes of the *SR3G* (RNAi line #04, targeting
620 AT3G50150, RNAi line #16 targeting AT3G50130, *SR3G*, and AT3G50170, and RNAi line #19 targeting
621 AT3G50130, AT3G50140, AT3G50150, *SR3G*, AT3G50170, AT3G50180, and AT3G50190). Three out of five
622 screened independent transformation lines from RNAi line #04 showed a decreased relative main root
623 length (Salt / Control, CSHL #4 B2a, D4a, and G1d), whereas two lines showed a decrease in relative lateral
624 root number (CSHL #4 D4a and F1b), and one line showed decreased lateral root length at 75 mM NaCl
625 (CSHL #4 D4a **Fig. S21-23**). Two out of two independent transformants for RNAi line #16 showed a
626 decreased relative main root length and increased lateral root number at 75 mM NaCl (CSHL #16 A2c and

B1a, **Fig. S21-23**). In three of the four screened independent transformants of line #19 we observed an increased lateral root length at 75 mM NaCl (CSHL #19 F1a, I3c, and L1c **Fig. S21-23**). We did not observe strong reduction in lateral root development across RNAi lines targeting two closely related DUF247 genes (i.e., RNAi line #22, targeting AT3G50150 and *SR3G*), as in the single mutant (**Fig. 6, Fig. S21**). The above results further support that these two genes do not act redundantly in the context of lateral root development.

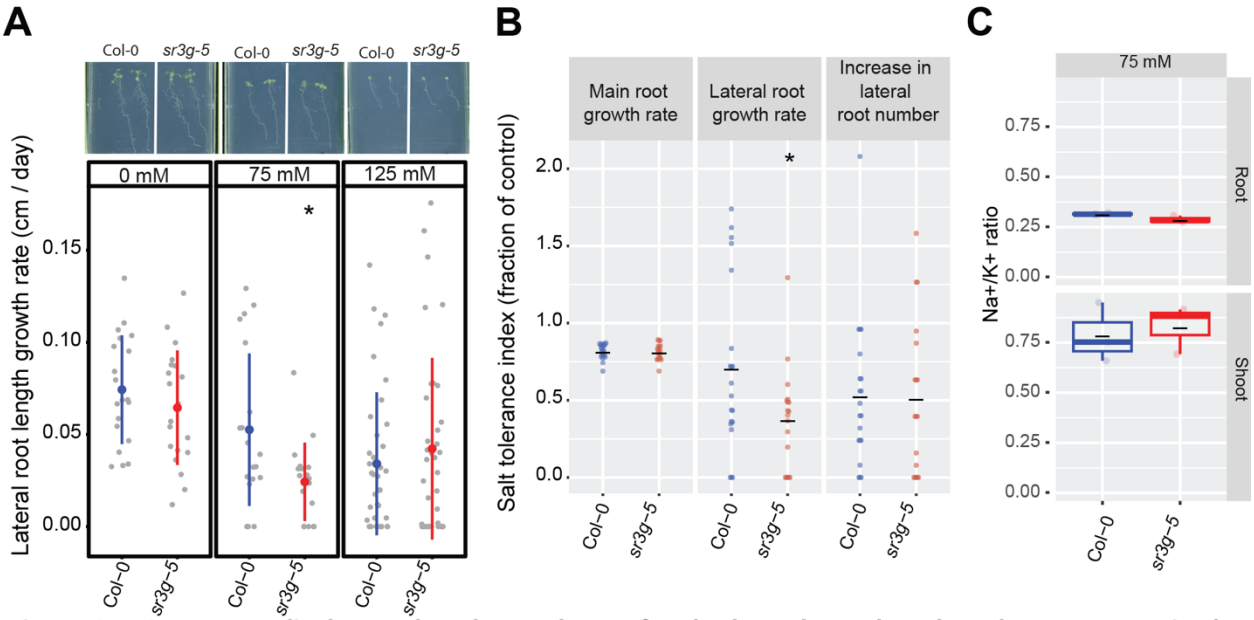

Figure 6. sr3g mutant displays reduced growth rate for the lateral root length and Na+ content in the root. Root system architecture analysis of Col-0 and sr3g-5 genotypes under various concentrations of NaCl are shown here. **(A)** Shown are representative images of 13-day-old Col-0 and sr3g-5 genotypes that experienced 9 days of salt treatment at indicated concentrations as well as growth rate for lateral root length. **(B)** Salt Tolerance Index (STI) for the main root length, average lateral root length, and lateral root number at 75 mM NaCl. The STI was calculated by dividing the growth rate measured under salt stress by the growth rate measured under control condition for each genotype. **(C)** Na+/K+ ratio in root and shoot of Col-0 and sr3g-5 after two weeks on 75 mM salt are shown. Each dot in (A) and (B) represents individual replicate per genotype. Lines in (A) and (B) graphs represent median and average, respectively. In (A) and (B), the asterisks above the graphs indicate significant differences between Col-0 and the sr3g-5 mutant, as determined by the Student 's t-test: *P < 0.05. Statistical analysis in (C) was done by comparison of the means for all pairs using Tukey–Kramer HSD test. Levels not connected by the same letter are significantly different (P < 0.05). Root system architecture and ICP-AES analyses of Col-0 and sr3g-5 mutant are shown in details in Figure S17.

Loss of *SR3G* results in increased salt tolerance in soil

To investigate *SR3G's* contribution to salt stress tolerance beyond seedling stage and agar plate conditions, we evaluated the performance of Col-0 and *sr3g-5* mutant in soil. We exposed the soil-grown plants to salt stress and imaged the rosette size every 30 minutes for two weeks using the automated imaging platform (Yu et al., 2023). As salt-induced changes depend on the developmental stage at which the stress is applied (Julkowska et al., 2017), we examined the role of *SR3G* exposed to salt stress at 2 or 3 weeks after germination, corresponding to early and late vegetative stages. We calculated a daily growth rate for each plant, using the projected rosette area. No significant difference was observed between Col-0 and *sr3g-5* under control conditions (**Fig. 7A-B**), indicating that *SR3G* does not play a role in plant development under non-stress conditions. Significant difference was observed between Col-0 and *sr3g-5*

644 for plants exposed to early salt treatment (**Fig. 7A-B**), where *sr3g-5* mutant displayed an increased rosette
645 growth rate as compared to Col-0 (**Fig. 7A**). Late stress exposure resulted in significantly higher *sr3g-5*
646 growth rate at two and three days after exposure to salt stress (**Fig. 6A**). Similarly, the *sr3g-5* mutant
647 showed a significantly higher rosette area compared to Col-0 exclusively when plants were exposed to
648 salt stress at an earlier stage of their development (**Fig. 7A**). No significant difference was observed
649 between Col-0 and *sr3g-5* mutant in terms of water content under either of conditions tested, providing
650 no substantial evidence for SR3G to to regulate water content (**Fig. S24**).
651 To investigate the role of *SR3G* in the maintenance of cellular integrity during salt stress, we
652 evaluated the salt-induced changes in cell membrane integrity by measuring ion leakage in the leaf discs
653 at the end of the experiment (**Fig. 7C**). While ion leakage increased in Col-0 under early salt stress
654 conditions, no noticeable salt-induced change was observed for *sr3g-5* compared to control condition
655 (**Fig. 7C**). Although the *sr3g-5* mutant exhibited significant increase in ion leakage in response to late salt
656 stress, this phenomenon may be more closely associated with the onset of senescence rather than direct
657 exposure to salt stress (**Fig. 7C**).
658 We further explored the role of *SR3G* in ion exclusion by quantifying the accumulation of Na^+ and
659 K^+ ions in the rosette at the end of the experiment (4-weeks-old plants). We observed a reduced
660 accumulation of Na^+ in *sr3g-5* mutants compared to Col-0 for plants exposed to salt stress at an earlier
661 timepoint (**Fig. 7D**). No significant differences in Na^+ accumulation was observed between the Col-0 and
662 *sr3g-5* at the late salt stress regime (**Fig. 7D**). A subtle, non-significant, reduction in K^+ content was
663 observed in *sr3g-5* mutant compared to Col-0 across all three conditions studied (**Fig. 7E**). In summary,
664 these results suggest that *SR3G* plays a negative role in maintenance of plant growth, cellular integrity
665 and Na^+ accumulation during the salt stress, especially when the salt stress is applied during early
666 vegetative development.

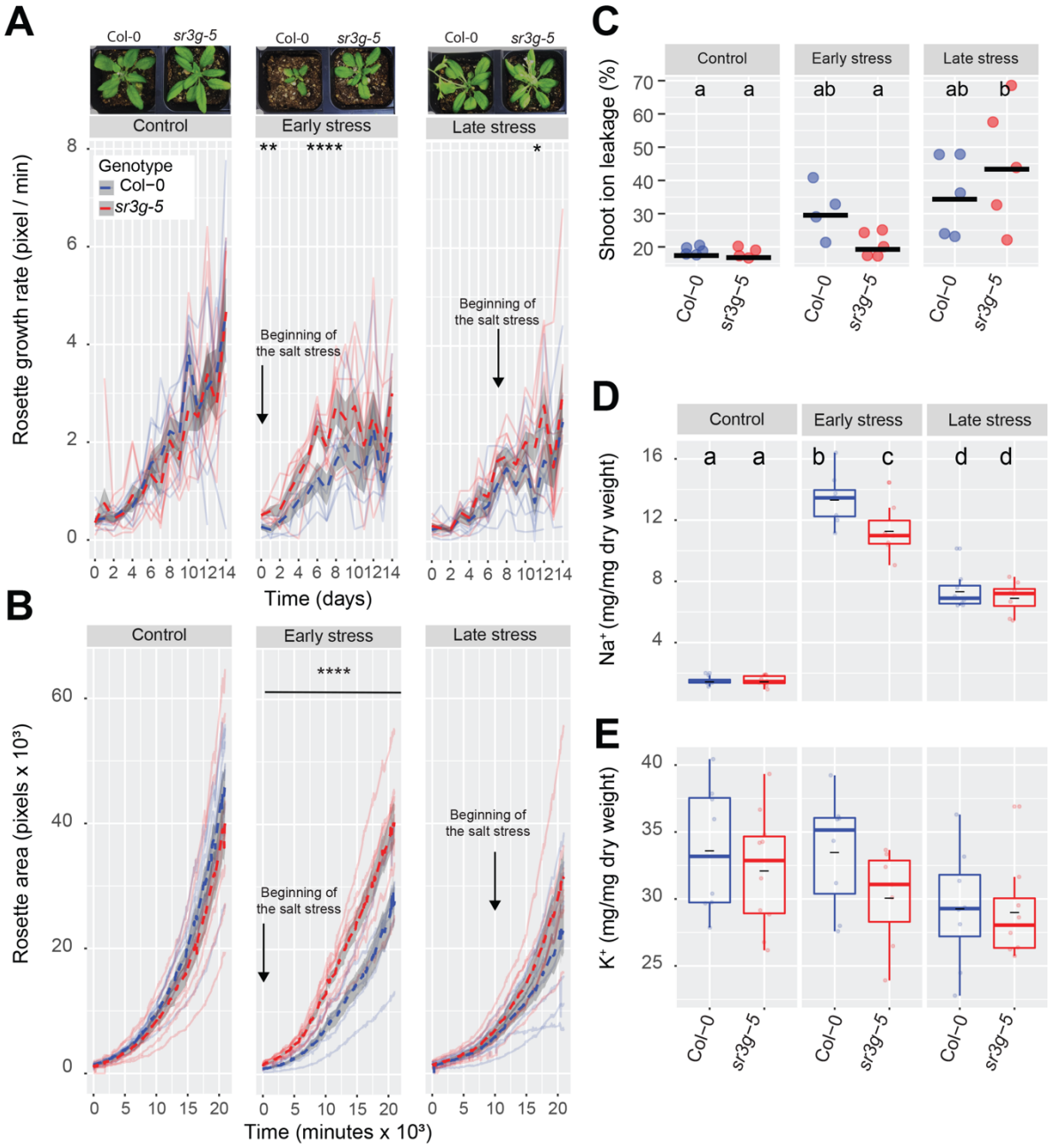

Figure 7. sr3g mutant has higher growth rate and larger rosette area while displaying less ion leakage and Na+ accumulation in shoot under salt stress. The salt stress responses of 2-week-old (referred to as "early salt stress") or 3-week-old (referred to as "late salt stress") soil-grown Col-0 and sr3g-5 plants that were exposed to a final concentration of 100 mM NaCl were examined here. **(A)** Rosette growth rate and **(B)** area were monitored over a period of two weeks, during which the "early salt stress" group experienced two weeks of salt stress while the "late salt stress" group experienced one week. Representative images of 4-week-old Col-0 and sr3g-5 genotypes were shown in (A). **(C)** Ion leakage percentage, **(D)** Na+ and **(E)** K+ contents in shoot were measured in 4-week-old plants. Each line in (A) and (B) represents the trajectory per genotype through time, where red and blue lines indicate Col-0 and sr3g-5 plants grown under control or salt-stress conditions, respectively. The dashed lines represent the mean values of the genotype per condition, whereas the grey band represents the confidence interval. The asterisks above the graphs indicate significant differences between Col-0 and sr3g-5 plants, as determined by one-way analysis of variance: *P < 0.05, **P < 0.01, ***P < 0.001, and ****P < 0.0001. Statistical analysis in (C) to (E) was done by comparison of the means for all pairs using Tukey–Kramer HSD test. Levels not connected by the same letter are significantly different (P < 0.05).

668 ***sr3g* mutant displays enhanced root suberization**

669 As *SR3G* limits shoot growth, promotes cell damage and sodium translocation into shoot (**Fig. 7**), and is
670 expressed in the most inner layers of the root (i.e., stele, **Fig. S13**), we hypothesized that *SR3G* plays a role
671 in the regulation of suberization within the Casparian strips located in the endodermis, the layer adjacent
672 to the stele. Salt stress exposure increases root suberization, thereby limiting Na^+ loading into the
673 transpiration stream and accumulation in the shoot (Baxter et al., 2009). We examined root suberization
674 patterns in Col-0 and *sr3g-5* under non-stress and salt stress conditions. Root suberization was visualized
675 using lipophilic stain Fluorol Yellow (FY), and staining intensity was examined under a confocal
676 microscope. Additionally, we examined the developmental transition in root suberization through imaging
677 four regions along the main root (**Fig. 8**). Visually, we observed that roots of *sr3g-5* were more suberized
678 compared to Col-0 under both control and salt stress conditions (**Fig. 8A**). The quantification of FY signal
679 intensity revealed non-significant, but substantially higher levels of root suberization in *sr3g-5* compared
680 to Col-0 in sections one to three of the root under control condition (**Fig. 8B**). Only in root section four,
681 the level of suberization significantly decreased in *sr3g-5* compared to Col-0 (**Fig. 8B**). In plants exposed
682 to salt stress, we observed a non-significant difference between *sr3g-5* and Col-0 throughout the four
683 sections, although, in section one which is the root tip proximal, *sr3g-5* showed more suberization
684 compared to Col-0 (section 1, **Fig. 8A**). These results suggest that *SR3G* may play a negative role in root
685 suberization.

686 To validate the FY histochemical analysis, we quantified root suberin monomers in the Arabidopsis
687 seedlings using GC-MS analysis. Suberin monomers that were detected in the Arabidopsis roots included
688 fatty acid (FA), fatty alcohol (OH-FA), α,ω-dicarboxylic acids (DCA), and ω-hydroxy fatty acid (ωOH-FA).
689 Roots of *sr3g-5* contained significantly more total FA and DCA monomers compared to Col-0 under control
690 condition, whereas the total OH-FA and ωOH-FA remained unchanged (**Fig. 8C**). In plants exposed to salt
691 stress, the *sr3g-5* mutant showed an increased abundance of three suberin monomers, with DCA and
692 ωOH-FA showing the most significant changes (**Fig. 8C**). The total FA decreased significantly in the mutant
693 compared to Col-0 (**Fig. 8C**). Together, these results further corroborate with FY staining, suggesting that
694 SR3G plays a negative role in root suberization.

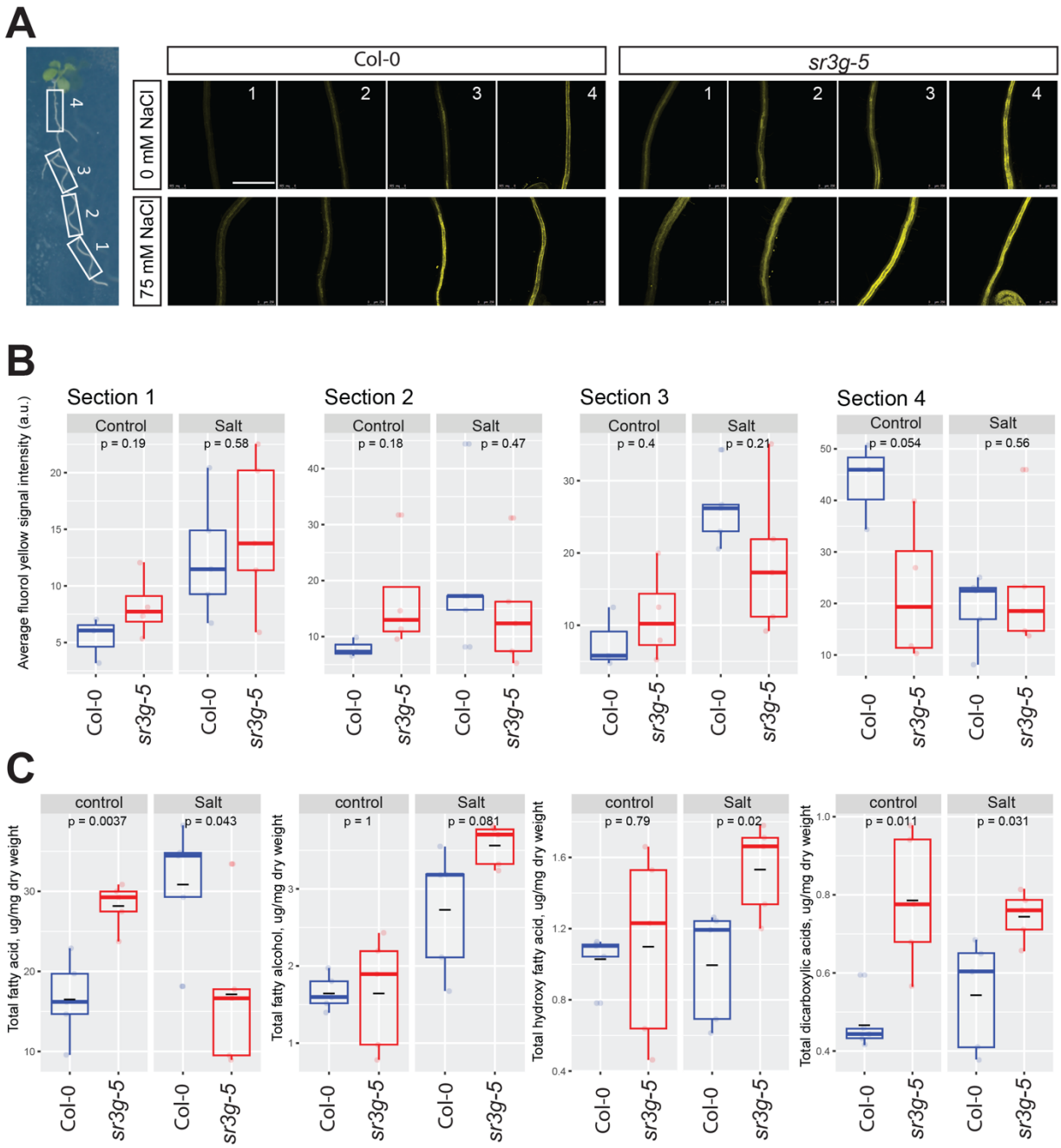

Figure 8. sr3g mutant root is more suberized than Col-0. (A) Representative images of fluorol yellow (FY) staining of four root sections (# 1 to 4, from root tip to root base as shown by white rectangles across the seedling) were shown for Col-0 and sr3g-5 mutant with or without 75 mM NaCl. Seeds were germinated on the 1/2 MS plates for 4 d and then seedlings were transferred to the treatment plates with or without 75 mM NaCl for 2 more days. **(B)** Quantification of FY signal intensity for each root section. The FY quantification was done using ImageJ. Scale bar is equal to 500 µm in all. **(C)** Suberin monomers detected using Gas Chromatography–Mass Spectrometry (GC-MS) in the Col-0 and sr3g-5 mutant roots with or without 75 mM NaCl included fatty acid (FA), fatty alcohol (OH-FA), α,ω-dicarboxylic acids (DCA), and ω-hydroxy fatty acid (ωOH-FA). The significant differences between Col-0 and sr3g-5 mutant were evaluated using Student 's t-test.

696 ***SR3G* expression is regulated by *WRKY75* transcription factor**

697 To identify potential transcriptional regulators of *SR3G*, we examined the *SR3G* promoter for cis-
698 regulatory elements using the CisCross tool (https://plamorph.sysbio.ru/ciscross/), and made a list of
699 transcription factors that putatively interact with *SR3G* promoter (**Fig. 9A**). As the root stele showed the
700 highest enrichment in the *SR3G* transcript (**Fig. S13**), we examined the transcription factors that were
701 previously identified to be expressed in root stele (Brady et al., 2011). Cross-referencing of these two
702 datasets revealed one transcription factor, *WKRY75* (AT5G13080) that was both enriched in root stele,
703 and potentially binding to *SR3G* promotor.
704 *WRKY75* was previously described to act as a positive regulator of salt stress response by
705 enhancing *SOS1* expression (Lu et al., 2023). To investigate whether the *SR3G* expression depends on
706 *WRKY75*, we examined the *SR3G* expression in the *wkry75* T-DNA insertion lines. *SR3G* expression was
707 undetected in *wrky75* loss-of-function mutants (**Fig. 9B**), suggesting that *WKRY75* regulates *SR3G*
708 expression. In comparison, expression of *WRKY75* remained unchanged in the *sr3g-5* mutant when
709 compared to Col-0 (**Fig. 9C**). To investigate whether *WRKY75* directly binds to the *SR3G* promoter, we
710 performed Y1H assay. Similar to the two positive controls, the strains transformed with WRKY75-AD and
711 SR3G:pLacZ grew on the SD/-Trp/-Ura + X-Gal medium, thereby confirming the interaction between
712 *WRKY75* and *SR3G* promoter region (**Fig. 9D**). In contrast, *WRKY75* did not show binding affinity to the
713 promoter region of the adjacent gene to the *SR3G* (i.e., DUF247-150, AT3g50150), thereby reinforcing the
714 uniqueness of the interaction between the *SR3G* and *WRKY75* (**Fig. 9E**).

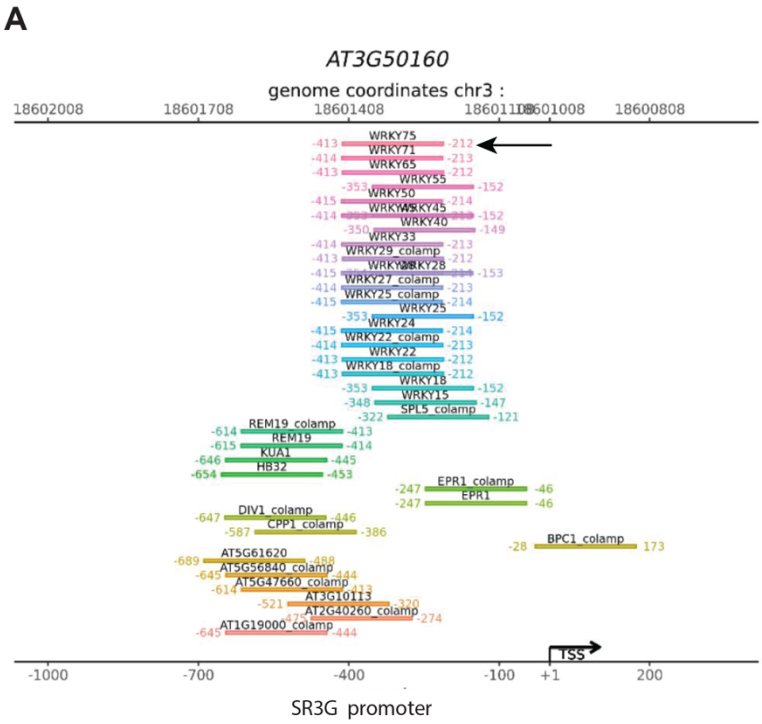

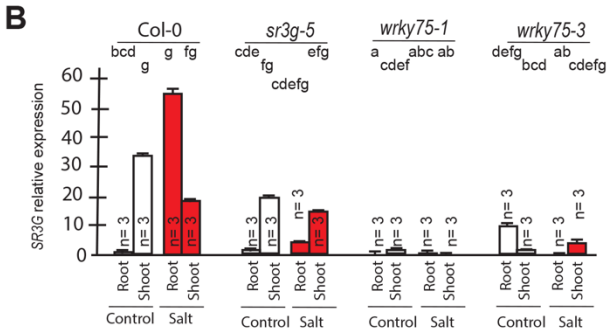

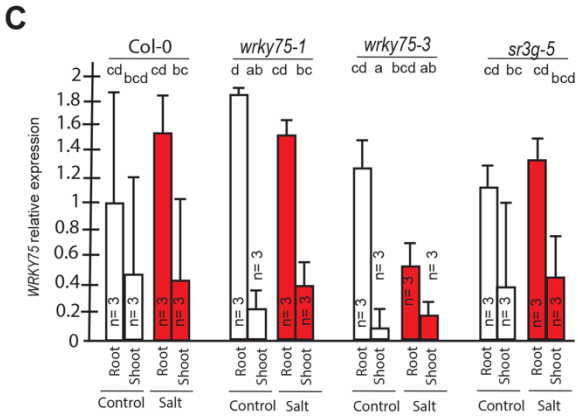

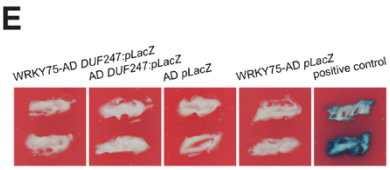

Figure 9. WRKY75 binds to the promoter region of the SR3G but not to its neighboring DUF247. (A) *In silico* searches in CisCross (https://plamorph.sysbio.ru/ciscross/CCL_index.html) shows potential transcription factors with binding sites on the main SR3G (At3g50160) promoter region. A black-arrow points to the WRKY75 (AT5G13080). RT-qPCR showing expression of SR3G (AT3G50160) **(B)** and WRKY75 (AT5G13080) **(C)** genes, respectively, in Col-0, sr3g-5 mutant, and two different mutant alleles of the wrky75, i.e., wrky75-1 and wrky75-3. RT-qPCR analyses were conducted using seedlings grown on 1/2x MS for 4 d and then followed by transferring to the treatment plates with or without 75 mM NaCl for one week. Mean values are shown ± SE, with three biological replicates used in each condition and genotype. AT4G04120 (transposable_element_gene) was used as a reference gene for normalization. Significance was determined by the Tukey–Kramer HSD test in JMP. Levels not connected by same letter are significantly different. Yeast one-hybrid (Y1H) assay showing WRKY75 (438 bp) binds to the promoter region of the main SR3G (AT3G50160, 953 bp) **(D)** but not to its neighboring promoter, i.e. DUF247-150 (At3g50150, 631 bp) **(E)**. pB42AD (AD) and pLacZ were used as effector and reporter construct, respectively. Effector and reporter constructs were co-transformed into yeast strain EGY48. Transformants were selected and grown on SD/-Trp-Ura medium. The interactions were observed on SD/-Trp/-Ura + X-Gal medium. Empty vector expressing AD domain and pLacZ were used as negative control. The two positive controls are NIGT1.4-GolS2 and NIGT1.4-GAE1. The oligo sequences used for Y1H and luciferase assays were provided in Table S4.

To further examine the functional consequences of the relationship between SR3G and WRKY75, we generated *wrky75-3/sr3g-5* double mutants, and examined their root system architecture alongside the single mutants and Col-0. Under control conditions, both *sr3g-5* and *wrky75-3* mutants showed significant reduction in main root length compared to Col-0 and the two double mutants (**Fig. 10A**). Under

75 mM salt, only *wrky75-3* showed significant reduction in main root length compared to all other genotypes tested, confirming the previously described salt sensitivity for *wrky75* mutant under salt stress (Lu et al., 2023). We have not observed any differences in main root length under 125 mM salt across all genotypes tested (**Fig. 10A**). Regarding lateral root number (**Fig. 10B**) and length (**Fig. 10C**), we observed significant reduction in lateral root number and length for the two single mutants, *sr3g-5* and *wrky75-3*, compared to other genotypes only under control condition (**Fig. 10B-C**). We further investigated Na^+ and K^+ accumulations as well as Na^+/K^+ ratio in plate grown seedlings (**Fig. 10D, Fig. S25, S26**). At 75 mM salt concentration, a subtle reduction in root Na^+/K^+ ratio was observed in the *wrky75* single mutant compared to the other genotypes tested. Conversely, shoot Na^+/K^+ ratio exhibited a slight decrease in the two double mutants compared to the other three genotypes at 75 mM salt concentration. At 125 mM salt concentration, root Na^+/K^+ ratio decreased in the two double mutants compared to Col-0 and the two single mutants. Similarly, the two double mutants maintained lower Na^+/K^+ ratios compared to Col-0 and the two single mutants in shoot at 125 mM salt concentration (**Fig. 10D**), indicating that the *SR3G* mutation indeed compensated for the increased Na^+ accumulation observed in the *wrky75* mutant under salt stress.

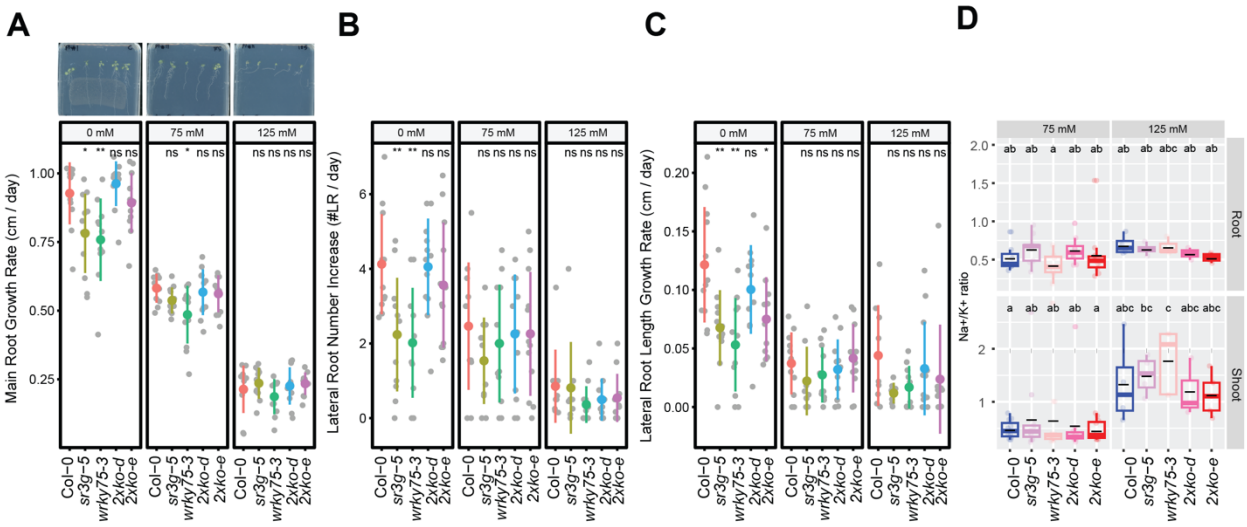

Figure 10. wrky75/sr3g double mutants roots exhibit reduced sensitivity to salt stress and accumulate lower levels of Na+ in their shoots. (A-C) Root system architecture analysis for the Col-0, sr3g-5, wrky75-3, and two double mutants under various concentrations of NaCl are shown here. Main root growth rate **(A)**, Lateral root number increase **(B)**, and Lateral root length increase **(C)** are shown for the indicated genotypes at various salt concentrations. **(D)** Na+/K+ ratio in root and shoot of indicated genotypes after two weeks on treatment plates. Each dot represents individual replicate per genotype. The asterisks above the graphs (A-C) indicate significant differences between Col-0 and the genotype, as determined by the Student 's t-test: *P < 0.05 and **P < 0.01. ns denotes no statistically significant. Statistical analysis in (D) was done by comparison of the means for all pairs using Tukey–Kramer HSD test. Levels not connected by the same letter are significantly different (P < 0.05).

Discussion

Exposure to abiotic stress alters plant architecture by affecting biomass distribution between individual organs (Guo et al., 2020; Julkowska and Testerink, 2015). Exposure to drought alters the distribution of the biomass between root and shoot, to optimize water uptake, while limiting transpiration (Asch et al., 2005; Chen et al., 2022; Karcher et al., 2008; Uga et al., 2013). While the processes underlying salt-induced changes in shoot and root growth dynamics and architecture have been systematically described (Ariel et al., 2010; Awlia et al., 2021; Deolu-Ajayi et al., 2019; Duan et al., 2013; Geng et al., 2013; Julkowska et al., 2017; Yutao Zou et al., 2022), the methodological exploration of biomass distribution between root and shoot for plants exposed to salt stress is underexplored in the current body of research. Here, we developed a tool that allows a non-destructive quantification of root and shoot projected area of the seedlings grown on agar plates (**Fig. 1A**). This new tool allows us to efficiently describe changes in biomass accumulation and stress-induced alterations in root and shoot growth. Although the method is restricted to small plants and early developmental stages, it provides valuable insight into stress responses. The application of this tool to an Arabidopsis natural diversity panel revealed that salt stress exposure results in loss of coordination between root and shoot growth (**Fig. 1D**), rather than a clear directional change, as in the case of drought. To our knowledge, this is the first systematic study of changes in root:shoot ratio. The developed tool for quantifying root and shoot size in plate-grown Arabidopsis has the potential to significantly advance research by enabling developmental and stress studies, focusing on coordination of root and shoot development during seedling establishment. Facilitating detailed comparisons of root:shoot ratios, this tool can aid in formulating new hypotheses about the mechanisms contributing to seedling vigor and stress tolerance.

The natural variation in salt-induced changes in root:shoot ratio revealed a clear association with SNPs on chromosome 3 within *SR3G*, that is situated within a region containing eight other *DUF247* genes (**Fig. 2**). SR3G was previously associated with self-incompatibility in grasses (Crain et al., 2020; Lian et al., 2021), as well as with lesions and dwarfism in Arabidopsis (Kondou et al., 2013) through constitutive activation of defense responses. However, the *SR3G* associated with constitutive defense response was AT3G60470 (Kondou et al., 2013), which is located outside the interval associated with salt stress-induced changes in root:shoot ratio (**Fig. 2C**). Because we did not observe any consistent phenotypes in the T-DNA insertion lines of *DUF247s* neighboring the *SR3G* (**Fig. S19-20**), we examined the RNAi lines targeting multiple *DUF247s* including *SR3G* (**Fig. S21-23**). Our root system architecture analyses revealed no redundancy between *SR3G* and other DUF247s, and the reduced lateral root development in double mutants of RNAi lines simply mimics the phenotype of *sr3g-5* single mutant (**Fig. 6, Fig. S21**). Further, we demonstrated that only *SR3G* is regulated by *WRKY75* (**Fig. 9B-E**). As these genes are result of tandem duplication, they are expected to accumulate a lot of variation in the cis-regulatory regions. Therefore, differential regulation of two closely related genes can be expected by the accumulated variation within the promoter region.

The results acquired in this study provide multiple layers of evidence that support the role of *SR3G* as a negative regulator of salt stress response in Arabidopsis. Loss-of-function *SR3G* maintained higher shoot growth rate and larger rosette area when exposed to salt stress in the soil (**Fig. 7A-B**), probably due to reduced Na^+ accumulation (**Fig. 7D**), which in turn resulted in lower rates of cellular damage (**Fig. 7C**). This increased salt tolerance feature can be explained by the increased root suberization (**Fig. 7**) as suberin-deficient mutants show susceptibility to salt stress (Barberon et al., 2016; Shukla et al., 2021; Ursache et al., 2021). For example, Arabidopsis *CYP86A1/HORST* (At5g58860) encodes a cytochrome P450-dependent enzyme that is responsible for catalyzing fatty acid ω-hydroxylation. It plays a pivotal role in the biosynthesis of aliphatic suberin, particularly expressed in the root endodermis. Knock-out mutations of *CYP86A1/HORST* result in a substantial decrease of approximately 60% in total root suberin

783 (Höfer et al., 2008; Li et al., 2007). Consequently, the diminished aliphatic suberin content in the roots of
784 *cyp86a1* mutants leads to increased permeability to water and solutes (Ranathunge and Schreiber, 2011).
785 Interestingly, *SR3G* expression is enhanced by salt stress (**Figs. 4, Fig. S13**), specifically in the root stele
786 (**Fig. S13B**). The root stele encompasses vascular bundles, procambium and pericycle, which gives rise to
787 the secondary growth and lateral root primordia respectively (Birnbaum et al., 2003). The stele is central
788 to the systemic transport of water, minerals, and nutrients within the plant (Li et al., 2017; Ramachandran
789 et al., 2020; Zarebanadkouki et al., 2019), and to the exclusion of salt ions from the transpiration stream
790 (Møller et al., 2009).
791 The deposition of hydrophobic residues of lignin and suberin in the Casparian strips poses a
792 significant barrier to apoplastic transport (Foster and Miklavcic, 2017). Previously, silencing genes involved
793 in Casparian strips formation resulted in increased lateral root development (Wang et al., 2020). As the
794 suberization of the Casparian strips increases upon salt stress, it limits the accumulation of Na^+ and loss
795 of K^+ ions from the root stele (Barberon et al., 2016). However, the effects of increased root suberization
796 under salt stress have thus far not been described to affect lateral root development. Here, we have
797 identified *SR3G* as a negative regulator of root suberization under salt stress (**Fig. 8**), which provides an
798 additional layer of protection against sodium accumulation (**Fig. 8**), but negatively impacts lateral root
799 development (**Fig. 6A-B**).
800 As SR3G was previously not described in the context of salt stress, we attempted to identify its
801 molecular context through its transcriptional regulation. Through our *in-silico* analysis, we have identified
802 *WRKY75* as a putative regulator of *SR3G* expression, and confirmed it using RT-qPCR and Y1H assay (**Fig.**
803 **9**). WRKY75 was previously described to act as a positive regulator of salt stress tolerance through
804 activation of *SOS1* expression (Lu et al., 2023). Similar to previous study, we also observed *wrky75* mutants
805 to be more sensitive to salt stress within our experiments (**Fig. 10A-C**). Nevertheless, when the *wrky75*
806 mutation was coupled with *sr3g-5*, the roots displayed a phenotype identical to Col-0 (**Fig. 10A**), implying
807 that the salt sensitivity of the *wrky75* mutant was counteracted by the *SR3G* mutation. Considering
808 *WRKY75's* role in positively regulating *SOS1* expression during salt stress, it is plausible that its binding to
809 the *SR3G* promoter inhibits its expression, thereby enhancing salt tolerance on a larger scale.
810 One of the main players in Na^+ transport is High-affinity K^+ Transporter (HKT1) (Laurie et al., 2002).
811 HKT1 is expressed in root stele (Mäser et al., 2002), where it retrieves Na^+ from the transpiration stream
812 and limits ion accumulation in the shoot, resulting in higher salt stress tolerance at later developmental
813 stages (Møller et al., 2009). At early developmental stages, *HKT1* overexpression reduces the
814 development of lateral root primordia (Julkowska et al., 2017), thus creating less Na^+ entry gate into the
815 main root, resulting in less Na^+ accumulation in shoot. Similarly, *sr3g-5* mutants developed fewer lateral
816 roots that are consistent with the lower Na^+ levels in the root upon salt stress (**Fig. 6**). The effects of HKT1
817 and SR3G differ in the magnitude of repression of lateral root development, with HKT1 mutants resulting
818 in almost complete cessation of lateral root development (Julkowska et al., 2017), whereas repression of
819 SR3G function has much more subtle phenotype. Whereas the effect of cell-type specific overexpression
820 of HKT1 on plant performance was negative during the early developmental stage, due to impairing lateral
821 root development, the *sr3g* mutants showed increased salt tolerance when exposed to salt stress
822 treatment during their early vegetative growth (**Fig. 7**). These results suggest that reduced lateral root
823 development under salt stress can have a gradient of responses leading to increased and decreased salt
824 tolerance, and the effect is highly dependent on the wider physiological mechanisms, and their
825 contributions to ion exclusion and maintained plant development throughout salt stress exposure.
826 In conclusion, the study of salt-induced changes in the root:shoot ratio, alongside the
827 development of new tools to quantify these changes during the seedling establishment stage, represents
828 an important new perspective into mechanisms underlying salt stress tolerance. Identification of SR3G as
829 a novel regulator of root suberization, shoot growth, and Na^+ accumulation provides better understanding

830 of molecular mechanisms underlying plant responses to salt stress, but also offers a new avenue to
831 explore more nuanced and tissue-specific strategies for enhancing salt stress tolerance.

832 # Acknowledgments

833 The authors would like to thank BTI and KAUST Greenhouse Teams for their care of the plants. The authors
834 would like to acknowledge support from the NSF-IOS #2023310 (ADLN) and NSF-IOS #2102120 (ADLN).
835 The majority of funding for this work was generously provided from KAUST baseline funding awarded to
836 Mark Tester, and BTI's startup funds awarded to Magdalena Julkowska.

837 ## Author contributions

838 M.M.J. and M.R.I. conceived the project and wrote the manuscript with inputs from all coauthors, C.T.
839 and M.A.T. helped with conceiving the overall idea for the project, infrastructure and funding, R.A.H and
840 R.S. developed the tool to quantify root and shoot size from Arabidopsis grown on agar plates, A.K.
841 assisted with GWAS analysis, M.R.I. conducted all experiments for functional characterization of *SR3G*,
842 H.S., and M.D.A. performed molecular cloning of DR3G, H.S. screened other DUF247s T-DNA and RNAi
843 mutant lines, L.J. performed the analysis of DUF247 domains that informed the cloning of individual SR3G
844 fragments, G.D. and M.W. conducted GC-MS on suberin monomers, M.P. and E.C. performed ICP-AES,
845 A.D.L.N. and L.Y. performed phylogenetic analysis, B.L. and Y.H. conducted Y1H.

846 ## Competing interests

847 The authors declare no competing interests

848 ## Correspondence and requests for materials

849 should be addressed to Dr. Magdalena M. Julkowska.

850 # Figure legends

851 **Figure 1. Salt stress is causing discoordination of root and shoot growth.** Arabidopsis HapMap population
852 was screened for salt stress-induced changes in root:shoot ratio. The increase in the projected area of
853 shoot and root (Fig. S2) was used to estimate **(A)** shoot and **(B)** root exponential growth rate. **(C)** The
854 root:shoot growth rate ratio was calculated per genotype. The histograms represent the number of
855 accessions across three studied conditions (0, 75 and 125 mM NaCl), whereas the population average is
856 indicated using the dashed line. Additionally, the distribution of the genotypes within each treatment was
857 visualized using the error plots (lower panel), where population average and standard error is indicated
858 using a colored point and a line, respectively. Individual grey points represent individual genotypes.

859 **Figure 2. SR3G is associated with salt stress-induced changes in shoot-per-total seedling area ratio.** The
860 salt induced changes in root-to-shoot and shoot-per-total seedling area ratios were used as an input for
861 GWAS. Manhattan plots representing the associations of shoot-per-total seedling area recorded 6 days
862 after transfer to 125 mM NaCl and **(A)** 250 k SNPs and **(B)** 4 M SNPs. **(C)** Significant associations were
863 found with the SNPs forming a locus on chromosome 3 in and around *SR3G* (AT3G50160), encoding
864 Domain of Unknown Function 247 (DUF247). The natural variation in the LD region was studied in 162
865 accessions sequenced by 1001 Genomes Project. The upper panel represents portion of the missing data,
866 upper middle panel represents deletions relative to Col-0, while lower middle panel represents the
867 sequence similarity compared to Col-0. The bottom panel represents the open reading frames (ORFs)
868 within the LD, and the location of associated SNPs is indicated with the dashed lines. Red dashed lines
869 represent associations above Bonferroni threshold in 250k SNP mapping, while grey lines represent
870 associations with -log10(p-value) > 5 in the 4M SNP mapping. **(D)** The haplotype analysis performed using
871 SNPs located within the coding region of the SR3G revealed significant differences in shoot-per-total
872 seedling area recorded 6 days after transfer to 125 mM NaCl between Haplotype groups 1 (represented
873 by 46 accessions, including Col-0) and 11 (represented by 11 accessions, including Blh-1). The significant
874 differences between individual haplotype groups were tested using ANOVA with Tukey HSD to identify
875 significantly different groups. **(E)** Upon further sequencing of SR3G in accessions from Haplotype 1 and
876 11, revealed two 200 bp insertions within SR3G exons in 4 tested accessions belonging to haplotype 11
877 group. These 200 bp insertions resulted in a premature STOP-codon within the DUF247 domain (after Gly-
878 215).

879

880 **Figure 3. Phylogeny and positive selection analysis of *SR3G* and its orthologs from other species.** The
881 orthologous genes of *SR3G* (AT3G50160) from other seven species were identified using GoGeBlast (E-
882 value < 1.00E-10). **(A)** The protein sequences of the 50 homologous genes were aligned by MUSCLE and
883 then an unrooted phylogenetic tree was reconstructed by a Maximum -likelihood (ML)-derived style by
884 RAxML (Bootstrap number: 100). **(B)** A positive selection analysis was conducted by branch-site model A
885 test: Specifically, we hypothesized the differential or constant dN/dS (ω) substitution rate among the
886 closely distant branches leading to DUF247 (AT3G50160) (See Method & Materials for details). These
887 branches were marked as ω1 (light brown branch), ω2 (DUF247-specific branch), ω3 (light blue branch),
888 and ω-rest (light purple branch). **(C)** The gene structure of DUF247 (AT3G50160) was illustrated by wide
889 arrows (grey arrow: 5 and 3' UTR, yellow arrow: coding-region). The regions used for cloning (Fragment
890 A, B, and C) were marked by narrow arrows along with "Coil-Coil Domain" and "Super-polar Fragment"
891 marked on Fragment A and B, respectively. Lastly, the Bayes Empirical Bayes (BEB) was performed to test
892 the probability of sites along with ω > 1 over the DUF247 (AT3G50160). Three sites were generated with
893 a posterior probability > 0.90: 124C (P = 0.992), 206A (P = 0.951), and 209A (P = 0.988). These three sites
894 were marked with an orange asterisk and assumed to have been undergoing positive selection.

895 **Figure 4. Transcript abundances for the two closely related *DUF247s.*** Expression of **(A)** *SR3G*
896 (AT3G50160) **(B)** and its closest homologue *DUF247-150* (AT3G50150) were measured in Col-0 seedlings
897 grown with and without salt stress. RT-qPCR analyses were conducted using seedlings grown on 1/2x MS
898 for 4 d and then followed by transferring to the treatment plates with or without 75 mM NaCl for one
899 week. Mean values are shown ± SE, with number of replicates (n) shown in each graph. *AT4G04120* was
900 used as a reference gene for normalization. Significance was determined by the Tukey–Kramer HSD test
901 in JMP.

902 **Figure 5. SR3G full-length protein resides in the plasma membrane while removal of its transmembrane**
903 **domain results in protein relocation to nucleus and cytosol.** SR3G full-length protein **(A-B)** or truncated
904 versions **(C-E)** fused to mVenus at the N-terminus were agro-infiltrated into the *Nicotiana benthamiana*
905 leaves for transient expression. Shown are a bright-field image of transfected leaf cells and mVenus-SR3G-
906 mediated fluorescence as well as GFP-based subcellular marker. **(A)** Localization of full-length SR3G alone
907 or **(B)** in combination with the known plasma membrane dye, FM4-64. Localization of truncated versions
908 of SR3G are shown for **(C)** SR3G-Fragment A, **(D)** SR3G-Fragment B, and **(E)** SR3G-Fragment AB. **(F)** Free
909 GFP was used as a nuclear and cytosolic marker. Scale bar = 25 µm.

910 **Figure 6. *sr3g* mutant displays reduced growth rate for the lateral root length and Na^+ content in the**
911 **root.** Root system architecture analysis of Col-0 and *sr3g-5* genotypes under various concentrations of
912 NaCl are shown here. **(A)** Shown are representative images of 13-day-old Col-0 and *sr3g-5* genotypes that
913 experienced 9 days of salt treatment at indicated concentrations as well as growth rate for lateral root
914 length. **(B)** Salt Tolerance Index (STI) for the main root length, average lateral root length, and lateral root
915 number at 75 mM NaCl. The STI was calculated by dividing the growth rate measured under salt stress by
916 the growth rate measured under control condition for each genotype. **(C)** Na^+/K^+ ratio in root and shoot
917 of Col-0 and *sr3g-5* after two weeks on 75 mM salt are shown. Each dot in (A) and (B) represents individual
918 replicate per genotype. Lines in (A) and (B) graphs represent median and average, respectively. In (A) and
919 (B), the asterisks above the graphs indicate significant differences between Col-0 and the *sr3g-5* mutant,
920 as determined by the Student 's t-test: $*P < 0.05$. Statistical analysis in (C) was done by comparison of the
921 means for all pairs using Tukey–Kramer HSD test. Levels not connected by the same letter are significantly
922 different ($P < 0.05$). Root system architecture and ICP-AES analyses of Col-0 and *sr3g-5* mutant are shown
923 in details in **Figure S17**.

924 **Figure 7. *sr3g* mutant has higher growth rate and larger rosette area while displaying less ion leakage**
925 **and Na^+ accumulation in shoot under salt stress.** The salt stress responses of 2-week-old (referred to as
926 "early salt stress") or 3-week-old (referred to as "late salt stress") soil-grown Col-0 and *sr3g-5* plants that
927 were exposed to a final concentration of 100 mM NaCl were examined here. Rosette growth rate **(A)** and
928 area **(B)** were monitored over a period of two weeks, during which the "early salt stress" group
929 experienced two weeks of salt stress while the "late salt stress" group experienced one week.
930 Representative images of 4-week-old Col-0 and *sr3g-5* genotypes were shown in (A). Ion leakage
931 percentage **(C)**, Na^+ **(D)** and K^+ **(E)** contents in shoot were measured in 4-week-old plants. Each line in (A)
932 and (B) represents the trajectory per genotype through time, where red and blue lines indicate Col-0 and
933 *sr3g-5* plants grown under control or salt-stress conditions, respectively. The dashed lines represent the
934 mean values of the genotype per condition, whereas the grey band represents the confidence interval.
935 The asterisks above the graphs indicate significant differences between Col-0 and *sr3g-5* plants, as
936 determined by one-way analysis of variance: $*P < 0.05$, $**P < 0.01$, $***P < 0.001$, and $****P < 0.0001$.
937 Statistical analysis in (C) to (E) was done by comparison of the means for all pairs using Tukey–Kramer HSD
938 test. Levels not connected by the same letter are significantly different ($P < 0.05$).

939 **Figure 8. *sr3g* mutant root is more suberized than Col-0. (A)** Representative images of fluorol yellow (FY)
940 staining of four root sections (# 1 to 4, from root tip to root base as shown by white rectangles across the

941 seedling) were shown for Col-0 and *sr3g-5* mutant with or without 75 mM NaCl. Seeds were germinated
942 on the 1/2 MS plates for 4 d and then seedlings were transferred to the treatment plates with or without
943 75 mM NaCl for 2 more days. **(B)** Quantification of FY signal intensity for each root section. The FY
944 quantification was done using ImageJ. Scale bar is equal to 500 µm in all. **(C)** Suberin monomers detected
945 using Gas Chromatography–Mass Spectrometry (GC-MS) in the Col-0 and *sr3g-5* mutant roots with or
946 without 75 mM NaCl included fatty acid (FA), fatty alcohol (OH-FA), α,ω-dicarboxylic acids (DCA), and ω-
947 hydroxy fatty acid (ωOH-FA). The significant differences between Col-0 and *sr3g-5* mutant were evaluated
948 using Student 's t-test.

949 **Figure 9. WRKY75 binds to the promoter region of the *SR3G* but not to its neighboring DUF247. (A)** In
950 silico searches in CisCross (https://plamorph.sysbio.ru/ciscross/CCL_index.html) shows potential
951 transcription factors with binding sites on the main *SR3G* (At3g50160) promoter region. A black-arrow
952 points to the *WRKY75* (AT5G13080). RT-qPCR showing expression of *SR3G* (AT3G50160) **(B)** and *WRKY75*
953 (AT5G13080) **(C)** genes, respectively, in Col-0, *sr3g-5* mutant, and two different mutant alleles of the
954 *wrky75, i.e., wrky75-1* and *wrky75-3*. RT-qPCR analyses were conducted using seedlings grown on 1/2x
955 MS for 4 d and then followed by transferring to the treatment plates with or without 75 mM NaCl for one
956 week. Mean values are shown ± SE, with three biological replicates used in each condition and genotype.
957 *AT4G04120* (transposable_element_gene) was used as a reference gene for normalization. Significance
958 was determined by the Tukey–Kramer HSD test in JMP. Levels not connected by same letter are
959 significantly different. Yeast one-hybrid (Y1H) assay showing *WRKY75* (438 bp) binds to the promoter
960 region of the main *SR3G* (AT3G50160, 953 bp) **(D)** but not to its neighboring promoter, i.e. DUF247-150
961 (At3g50150, 631 bp) **(E)**. *pB42AD* (AD) and *pLacZ* were used as effector and reporter construct,
962 respectively. Effector and reporter constructs were co-transformed into yeast strain EGY48.
963 Transformants were selected and grown on SD/-Trp-Ura medium. The interactions were observed on SD/-
964 Trp/-Ura + X-Gal medium. Empty vector expressing AD domain and *pLacZ* were used as negative control.
965 The two positive controls are NIGT1.4-GolS2 and NIGT1.4-GAE1. The oligo sequences used for Y1H and
966 luciferase assay were provided in **Table S4.**

967 **Figure 10. *wrky75/sr3g* double mutants roots exhibit reduced sensitivity to salt stress and accumulate**
968 **lower levels of Na^+ in their shoots. (A-C)** Root system architecture analysis for the Col-0, *sr3g-5, wrky75-*
969 *3,* and two double mutants under various concentrations of NaCl are shown here. Main root growth rate
970 **(A)**, Lateral root number increase **(B)**, and Lateral root length increase **(C)** are shown for the indicated
971 genotypes at various salt concentrations. **(D)** Na^+/K^+ ratio in root and shoot of indicated genotypes after

two weeks on treatment plates. Each dot represents individual replicate per genotype. The asterisks above the graphs (A-C) indicate significant differences between Col-0 and the genotype, as determined by the Student 's t-test: *$P < 0.05$ and **$P < 0.01$. ns denotes no statistically significant. Statistical analysis in (D) was done by comparison of the means for all pairs using Tukey–Kramer HSD test. Levels not connected by the same letter are significantly different ($P < 0.05$).

977 # Supplemental Figure and Table Legends

978 **Figure S1. Evaluation of the tool's precision for estimating seedling size.** The tool used to quantify root
979 and shoot size from the agar plates was tested on the Arabidopsis Col-0 seedlings exposed to various
980 concentrations of salt stress (0, 75 and 125 mM NaCl). The fresh weight of root and shoot of individual
981 plants were recorded at the last day of experiment (8 days after transfer to treatment plates, 12 days after
982 germination), and the correlation analysis between individual organ's fresh weight and area was
983 performed in R. The Correlation co-efficient and the p-value for individual correlations were calculated in
984 R using stats package.

985 **Figure S2. Salt stress reduced the increase in root and shoot area over time across HapMap accession.**
986 Four-days-old seedlings exposed to 0, 75 and 125 mM NaCl grown on agar plates were scanned every 2nd
987 day and analyzed for root and shoot area using a custom tool. The change in genotype-specific **(A)** shoot
988 and **(B)** root area was calculated in R using stats package. The thick dashed lines represent population-
989 wide average in root and shoot area over the time of the experiment, while individual transparent lines
990 indicate change in root and shoot area for individual accession. The differences between control and
991 individual salt stress treatments were evaluated using ANOVA. The *, **, *** and **** represent p-values
992 below 0.05, 0.01, 0.001 and 0.0001 respectively.

993 **Figure S3. Salt stress induced changes in relative growth of shoot, root and root:shoot ratio.** The stress
994 tolerance index was calculated for shoot, root and root:shoot ratio by dividing genotype specific value
995 recorded at salt stress over the genotypic mean of the trait recorded under non-stress conditions.
996 Individual points represent individual genotypes. The population mean for 75 and 125 mM NaCl treated
997 plants is represented by the colored point, whereas the population-wide standard error.

998 **Figure S4. The correlation between all measured traits and calculated stress tolerance indices (STI).** The
999 correlations between all measured and calculated traits was performed using the Pearson's correlation
1000 coefficient. All non-significant correlations were replaced by blank circles. The size and color of individual
1001 circles indicates the strength and significance of individual correlation between two traits. Blue and red
1002 shades indicate positive and negative correlations respectively.

1003 **Figure S5. The correlation between total seedling area and salt-induced changes in the root-to-shoot**
1004 **ratio.** The correlation between the total seedling area quantified using the custom tool at the last day of
1005 experiment (8 days after transfer and 12 days after germination), and the ratio of root-and-shoot growth

1006 rate was examined across Arabidopsis HapMap population and various concentrations of salt stress (0, 75
1007 and 125 mM NaCl). The correlation analysis was performed in R, and the Correlation co-efficient (r) and
1008 the p-values for individual correlations were calculated in R using stats package.

1009 **Figure S6. Region around NTL8 is associated with salt stress-induced changes in root-per-shoot growth.**
1010 The salt induced changes in root-to-shoot and shoot-per-total seedling area ratios were used as an input
1011 for GWAS. **(A)** Manhattan plot represents the associations of root-per-shoot growth factors recorded at
1012 75 mM NaCl with 250 k SNPs while **(B)** represents the QQ plot for this association study. **(C)** Significant
1013 associations were found with the SNPs forming a locus on chromosome 2 in and around AT2G27300,
1014 encoding a NAC-domain containing transcription factor (NTL8). The natural variation in the LD region was
1015 studied in 162 accessions sequenced by 1001 Genomes Project. The upper panel represents portion of
1016 the missing data, upper middle panel represents deletions relative to Col-0, while lower middle panel
1017 represents the sequence similarity compared to Col-0. The bottom panel represents the open reading
1018 frames (ORFs) within the LD, and the location of associated SNPs is indicated with the dashed lines. Red
1019 dashed lines represent associations above Bonferroni threshold in 250k SNP mapping, while grey lines
1020 represent associations with -log10(p-value) > 5 in the 4M SNP mapping.

1021 **Figure S7. Region around unknown gene is associated with salt stress-induced changes in relative**
1022 **changes in shoot-per-total seedling area.** The salt induced changes in root-to-shoot and shoot-per-total
1023 seedling area ratios were used as an input for GWAS. **(A)** Manhattan plot represents the associations of
1024 relative change (125 mM / 0 mM) in shoot-per-total seedling area at 4 days after transfer to 125 mM NaCl,
1025 while **(B)** represents the QQ plot for this association study. **(C)** Significant associations were found with
1026 the SNPs forming a locus on chromosome 3 in and around AT3G22430, encoding an unknown gene
1027 encoding a domain of unknown function. The natural variation in the LD region was studied in 162
1028 accessions sequenced by 1001 Genomes Project. The upper panel represents portion of the missing data,
1029 upper middle panel represents deletions relative to Col-0, while lower middle panel represents the
1030 sequence similarity compared to Col-0. The bottom panel represents the open reading frames (ORFs)
1031 within the LD, and the location of associated SNPs is indicated with the dashed lines. Red dashed lines
1032 represent associations above Bonferroni threshold in 250k SNP mapping, while grey lines represent
1033 associations with -log10(p-value) > 5 in the 4M SNP mapping.

1034 **Figure S8. The QQ-plots for GWAS models with shoot-per-total seedling area.** The QQ-plots for
1035 association between shoot-per-total seedling area recorded 6 days after transfer to 125 mM NaCl and **(A)**

1036 250 k SNPs and **(B)** 4 M SNPs. The red line indicates the expected vs. observed ratio of association, while
1037 black points indicate the observed associations.

1038 **Figure S9. Haplotype analysis of AT3G50160 (SR3G).** The haplotype analysis performed using SNPs
1039 located within the coding region of the SR3G (AT3G50160) revealed significant differences in **(A)** Relative
1040 shoot growth (as fraction of shoot growth at 125 mM NaCl and 0 mM NaCl) and **(B)** Shoot growth at 125
1041 mM NaCl. The significant differences between individual haplotype groups (each haplotype represented
1042 by at least 3 accessions), were tested using ANOVA with Tukey HSD to identify significantly different
1043 groups. Significant differences were identified between Haplotype groups 1 (represented by 46
1044 accessions, including Col-0) and 11 (represented by 11 accessions, including Blh-1).

1045 **Figure S10. Nucleotide sequence alignment of SR3G CDS between Col-0 and Blh-1 alleles.** The nucleotide
1046 sequences from SR3G CDS were obtained from Col-0 and Blh-1 cDNA, and compared to Col-0 cDNA
1047 sequence on TAIR. The cDNA sequences were subsequently aligned in JalView using ProbconsWS
1048 alignment. The intensity of purple hue indicates the nucleotide identity, while dash marks indicate
1049 insertion in Blh-1 compared to Col-0 allele.

1050 **Figure S11. Amino acid sequence alignment of SR3G CDS between Col-0 and Blh-1 alleles.** The amino
1051 acid sequences from SR3G CDS were obtained by translating Col-0 and Blh-1 cDNA into amino acid
1052 sequence in JalView using Standard settings. The amino acid sequences were subsequently aligned in
1053 JalView using ProbconsWS alignment. The sequence length markers for are indicated above the aligned
1054 sequence. The intensity of purple hue is indicating the nucleotide identity, while dash marks indicate
1055 insertion in one of the alleles. * indicate STOP codons.

1056 **Figure S12. Sequence alignment between Col-0 and Blh-1 alleles for SR3G promotor.** The nucleotide
1057 sequences from SR3G promotor were obtained from Col-0 and Blh-1 genomic DNA, and compared to Col-
1058 0 sequence on TAIR. The gDNA sequences were subsequently aligned in JalView using ProbconsWS
1059 alignment. The intensity of purple hue is indicating the nucleotide identity, while dash marks indicate
1060 insertions.

1061 **Figure S13. Gene expression profile of *SR3G* across various developmental stages and salt stress.** The
1062 absolute gene expression of *SR3G* is depicted across various developmental stages **(A)**, root cell types **(B)**,
1063 and in response to salt-induced changes **(C)**. The images were acquired through the eFP Browser using
1064 data sources specified for the developmental map, abiotic stress, and tissue specific.

1065 **Figure S14. Gene expression profile of other *DUF247s* under salt stress.** Absolute gene expression of
1066 other *DUF247s* are depicted in response to salt-induced changes. The images were acquired through the
1067 eFP Browser using data sources specified for the abiotic stress. The *SR3G* is shown in a green box for
1068 comparison.

1069 **Figure S15. SR3G predicted protein domains.** The SR3G protein sequence (Col-0 allele) was used to
1070 identify predicted protein domains. The identified domains include: nuclear localization signal (NLS): K15-
1071 F19; coiled-coil domain: M153-K173; potential Ca2+ binding pocket: G210-F372; and transmembrane
1072 domain P469-T503. Informed by these predicted protein domains, we designed SR3G Fragment A, B and
1073 C for subsequent localization studies and functional characterization. The pink mark at Y216 indicates a
1074 position of a premature STOP codon in Blh-1 allele.

1075 **Figure S16. The expression of *DUF247-150* remains unaltered in the *sr3g* mutant. (A)** Schematic diagram
1076 of main *SR3G* gene model and the location of T-DNA insertions. The location of T-DNA insertions is shown
1077 for *sr3g-4*, and *-5* mutants using triangles. RT-qPCR showing expression of *SR3G* gene (AT3G50160) **(B)**
1078 and its neighboring gene, *DUF247-150* (At3g50150) **(C)** in Col-0 and two *sr3g* mutants. RT-qPCR analyses
1079 were conducted using seedlings grown on 1/2x MS for 4 d and then followed by transferring to the
1080 treatment plates with or without 75 mM NaCl for one week. Mean values are shown ± SE, with the number
1081 of replicates (n) shown in each graph. *AT4G04120* (transposable_element_gene) was used as reference
1082 gene for normalization. Significance was determined by the Tukey–Kramer HSD test in JMP. Levels not
1083 connected by same letter are significantly different.

1084 **Figure S17. *sr3g-5* mutant displays no difference in main root length and lateral root numbers compared**
1085 **to Col-0.** Root system architecture analysis of Col-0 and *sr3g-5* genotypes under various concentrations
1086 of NaCl are shown here for main root length **(A)** and increase in lateral root number **(B)**. 13-day-old Col-0
1087 and *sr3g-5* genotypes experienced 9 days of salt treatment at indicated concentrations were used here.
1088 Each dot in (A) and (B) represents individual replicate per genotype. Statistical analysis was performed
1089 between Col-0 and the *sr3g-5* mutant using the Student 's t-test: $*P < 0.05$. **(C)** Na^+, **(D)** K^+ contents in root
1090 and shoot of Col-0 and *sr3g-5* after two weeks on 75 mM salt are shown. Statistical analysis in **(C-D)** was
1091 done by comparison of the means for all pairs using Tukey–Kramer HSD test. Levels not connected by the
1092 same letter are significantly different ($P < 0.05$).

1093 **Figure S18. *sr3g-4* mutant has no alteration in root system architectures compared to Col-0.** Root system
1094 architecture analysis of Col-0 and *sr3g-4* genotypes under various concentrations of NaCl are shown here

1095 for main root length **(A)**, lateral root length **(B)**, and lateral root number **(C)**. Salt Tolerance Index (STI) for
1096 the main root length, average lateral root length, and lateral root number are shown at 75 **(D)** and 125 **(E)**
1097 mM NaCl, respectively. The STI was calculated by dividing the growth rate measured under salt stress by
1098 the growth rate measured under control condition for each genotype. Statistical analysis was performed
1099 between Col-0 and the *sr3g-4* mutant using the Student 's t-test: *$P < 0.05$.

1100 **Figure S19. Root system architecture analysis of neighboring DUF247 mutants under the salt.** Main root
1101 length **(A)**, lateral root number **(B)**, and lateral root length **(C)** are shown for neighboring *DUF247s* of the
1102 *SR3G*, including At3g50120 (shown as 120, with one T-DNA representative, 120-2(SAIL_382_A09)),
1103 At3g50140 (shown as 140, with three T-DNA representatives, 140-1 (SALK_044685), 140-2
1104 (SALK_005466), and 140-3 (SALK_122700)), At3g50150 (shown as 150, with two T-DNA representatives,
1105 150-1 (SALK_003824) and 150-3 (SALK_071080)), and At3g50170 (shown as 170, with two T-DNA
1106 representatives, 170-1 (SALK_009186) and 170-2 (SALK_112602)) compared to Col-0 under various
1107 concentrations of NaCl as indicated. The corresponding Salt Tolerance Index (STI) was calculated for main
1108 root growth **(D)**, increase in lateral root number **(E)**, and lateral root length **(F)**. Statistical analysis was
1109 performed between Col-0 and the other mutants using the Student 's t-test: *$P < 0.05$. The root system
1110 architecture analysis was performed similar to what described for Figure 6.

1111 **Figure S20. Root system architecture analysis of neighboring DUF247 mutants under the salt, continues.**
1112 Main root length **(A)**, lateral root number **(B)**, and lateral root length **(C)** are shown for neighboring of the
1113 *SR3G*, including At3g50170 (shown as 170, with three T-DNA representatives, 170-3F (SALK_008710), 170-
1114 4F (SALK_145999), 170-5A (SALK_072937)), At3g50190 (shown as 190, with one T-DNA representative,
1115 190-2B (SALK_137791)), and At3g50200 (shown as 200, with three T-DNA representatives, 200-1A
1116 (SALK_113759), 200-2B (SALK_093701), and 200-3B (SALK_129634)) compared to Col-0 under various
1117 concentrations of NaCl as indicated. The corresponding Salt Tolerance Index was calculated for main root
1118 growth **(D)**, increase in lateral root number **(E)**, and lateral root length **(F)**. Statistical analysis was
1119 performed between Col-0 and the other mutants using the Student 's t-test: *$P < 0.05$. The root system
1120 architecture analysis was performed similar to what described for Figure 6.

1121 **Figure S21. Root system architecture analysis of RNAi lines targeting neighboring DUF247s.** Main root
1122 length **(A)**, main root length tolerance index **(B)**, lateral root length **(C)**, lateral root length tolerance index
1123 **(D)**, lateral root number **(E)**, and lateral root number tolerance index **(F)** are shown for RNAi lines targeting
1124 AT3G50140 (CSHL3-F1a), targeting AT3G50130 and AT3G50140 (CSHL6-C2d), targeting AT3G50150 and

1125 AT3G50170 (CSHL11-F1b), targeting AT3G50140 and AT3G50170 (CSHL13-F2a), targetingAT3G50150 and
1126 AT3G50190 (CSHL18-K4c), targeting AT3G50130, AT3G50140, AT3G50150, AT3G50160, AT3G50170,
1127 AT3G50180, and AT3G50190 (CSHL19-E2c), targeting AT3G50130 and AT3G50150 (CSHL21-E2a), and
1128 targeting AT3G50150 and AT3G50160 (CSHL22-F1c). Statistical analysis was performed between Col-0 and
1129 the RNAi lines using a Student's t-test: *$P < 0.05$, **$P < 0.01$, ***$P < 0.001$, ****$P < 0.0001$.

1130 **Figure S22. Root system architecture analysis of RNAi lines targeting neighboring DUF247s continued.**
1131 Main root length **(A)**, main root length tolerance index **(B)**, lateral root length **(C)**, lateral root length
1132 tolerance index **(D)**, lateral root number **(E)**, and lateral root number tolerance index **(F)** are shown for
1133 RNAi lines targeting AT3G50160 (CSHL4-B2a and CSHL4G1d), targeting AT3G50140 and AT3G50150
1134 (CSHL7-A3a), targeting AT3G50140 and AT3G50190 (CSHL8-G2b), targeting AT3G50180 (CSHL10-I1c),
1135 targeting AT3G50130, AT3G50140, AT3G50170, AT3G50180, and AT3G50190 (CSHL12-A1a), targeting
1136 AT3G50140, AT3G50170, AT3G50180, and AT3G50190 (CSHL15-E1b), targeting AT3G50130, AT3G50160,
1137 and AT3G50170 (CSHL-A2c and CSHL16-B1a), targeting AT3G50130 and AT3G50160 (CSHL20-G3b), and
1138 targeting AT3G50130 and AT3G50150 (CSHL21-L2c and CSHL21-M1d). Statistical analysis was performed
1139 between Col-0 and the RNAi lines using a Student's t-test: *$P < 0.05$, **$P < 0.01$, ***$P < 0.001$, ****$P <$
1140 0.0001.

1141 **Figure S23. Root system architecture analysis of RNAi lines targeting neighboring DUF247s continued.**
1142 Main root length **(A)**, main root length tolerance index **(B)**, lateral root length **(C)**, lateral root length
1143 tolerance index **(D)**, lateral root number **(E)**, and lateral root number tolerance index **(F)** are shown for
1144 RNAi lines targeting AT3G50140 (CSHL3-F3a), targeting AT3G50160 (CSHL4-D1c3, CSHL4-D4a, and CSHL4-
1145 F1b), targeting AT3G50130 and AT3G50170 (CSHL5-D3b and CSHL5-E2b), targeting AT3G50130 and
1146 AT3G50140 (CSHL6-B1c), targeting AT3G50140 and AT3G50150 (CSHL7-C1b2), targeting AT3G50140 and
1147 AT3G50190 (CSHL8-D3b and CSHL8-H1d), targeting AT3G50180 (CSHL10-I1b), targeting AT3G50150 and
1148 AT3G50170 (CSHL11-E5b), targeting AT3G50130, AT3G50140, AT3G50170, AT3G50180, and AT3G50190
1149 (CSHL12-B1a and CSHL12-D1c), targeting AT3G50140 and AT3G50170 (CSHL13-F1b and CSHL13-F4d),
1150 targeting AT3G50140, AT3G50170, AT3G50180, and AT3G50190 (CSHL15-G1a1 and CSHL15-H2b),
1151 targeting AT3G50150 and AT3G50190 (CSHL18-E4c and CSHL18-I2d), targeting AT3G50130, AT3G50140,
1152 AT3G50150, AT3G50160, AT3G50170, AT3G50180, and AT3G50190 (CSHL19-F1a, CSHL19-I3c, and
1153 CSHL19-L1c), and targeting AT3G50130 and AT3G50160 (CSHL20-F2b). Statistical analysis was performed
1154 between Col-0 and the RNAi lines using a Student's t-test: *$P < 0.05$, **$P < 0.01$, ***$P < 0.001$, ****$P <$
1155 0.0001.

1156 **Figure S24. Plant water content comparison shows no significant differences between sr3g mutant and**
1157 **Col-0 wild-type plants.** Plant water content was calculated by subtracting rosette dry weight from fresh
1158 weight for the 2-week-old (referred to as "early salt stress") or 3-week-old (referred to as "late salt stress")
1159 soil-grown Col-0 and sr3g-5 plants that were exposed to a final concentration of 100 mM NaCl. "early salt
1160 stress" group experienced two weeks of salt stress while the "late salt stress" group experienced one
1161 week. Statistical analysis was done by comparison of the means for all pairs using Tukey–Kramer HSD
1162 test. Levels not connected by the same letter are significantly different (P < 0.05).

1163 **Figure S25. *wrky75/sr3g* double mutants exhibit higher shoot K^+ contents compared to Col-0 and each**
1164 **individual single mutant in the presence of 125 mM salt. (A)** Na^+ and **(B)** K^+ contents in root and shoot
1165 of Col-0, *sr3g-5, wrky75-3,* and two double mutants under various concentrations of NaCl are shown here.
1166 Statistical analysis in (A-B) was done by comparison of the means for all pairs using Tukey–Kramer HSD
1167 test. Levels not connected by the same letter are significantly different (*P* < 0.05).

1168 **Figure S26. *wrky75/sr3g* double mutants exhibit no noticeable differences in rosette area compared to**
1169 **their individual single mutants when grown in saline soil.** The salt stress responses of 2-week-old soil-
1170 grown plants that were exposed to a final concentration of 100 mM NaCl were examined here. Rosette
1171 area **(A)** and growth rate for each individual day were shown **(B-M)**. Growth rate is shown for 1 **(B)**, 2 **(C)**,
1172 and 3 **(D)** days before the stress, respectively. Growth rate is shown for 1 **(E)**, 2 **(F)**, 3 **(G)**, 4 **(H)**, 5 **(I)**, 6 **(J)**,
1173 7 **(K)**, 8 **(L)**, and 9 **(M)** days of stress application, respectively. Na+/K+ **(N)** ratio in shoot were measured in
1174 4-week-old plants. Each line in (A) represents the trajectory per genotype through time. The effect of the
1175 genotype within individual treatment in (B-M) was tested using ANOVA, and the significantly different
1176 genotypes were additionally determined using Tukey HSD test (pvalue < 0.05). Statistical analysis in (N)
1177 was done by comparison of the means for all pairs using Tukey–Kramer HSD test. Levels not connected by
1178 the same letter are significantly different (*P* < 0.05).

1179 **Table S1. The individual traits recorded and calculated from the HapMap accessions exposed to the**
1180 **three different levels of salt stress.** The root and shoot projected area were quantified using a custom
1181 developed tool. The change in the root and shoot area over time was used to calculate Growth Factor (GF)
1182 by fitting an exponential function. The broad sense heritability (H2) was calculated for each trait over
1183 individual days and conditions using MVApp.

1184 **Table S2. Genotypic mean data used as an input for GWAS.** The genotypic mean data was calculated
1185 from at least 4 biological replicates per genotype per condition. The root and shoot area were extracted

1186 using a custom developed tool. The Growth Factors (GF) for root and shoot were calculated using
1187 exponential growth function. Total seedling slze (Tot) was calculated by adding root and shoot area for
1188 individual day. Shoot per Total (SpT) ratio was calculated for individual days by dividing genotype specific
1189 shoot area by the total seedling area for that day and condition. Root per Shoot ratio (RpS) was calculated
1190 by dividing genotype specific root area by the shoot area for that day and condition.

1191 **Table S3. Significant associations identified with GWAS of all used traits.** The location of individual SNPs
1192 is listed according to its location on Chromosome (Chr) and position (Pos). The individual SNP Minor Allele
1193 Count (MAC) and Minor Allele Frequency (MAF) is calculated based on specific SNP set used (4 Million or
1194 250 Thousand – listed in "Mapping" column). The traits associated with individual SNPs are abbreviated
1195 as RpS for Root-per-Shoot, SpT for Shoot-per-Total seedling area, Tot for Total seedling area, GR for
1196 growth rate and SHIIT for Shoot Ion Independent Tolerance index (Salt / Control).

1197 **Table S4. Most important GWAS associations.** The most important associations identified through GWAS
1198 (Table S3) were inspected further for their functions using either T-DNA or RNAi mutant lines. List of
1199 oligoes used for genotyping, RT-qPCR, cloning, and Y1H assay are provided.

1200 **Table S5. The gene ID, species, and gene names used for identification of SR3G orthologs and**
1201 **paralogs.**

1202 **Table S6. Background and foreground values of omega.**

1203 **Table S7. Links to cloning construct maps generated in this study.**

1204

1205 # References

1206 1001 Genomes Consortium. 1001 Genomes Consortium. 2016. 1,135 Genomes Reveal the Global
1207 Pattern of Polymorphism in Arabidopsis thaliana. *Cell* **166**:481–491. doi:10.1016/j.cell.2016.05.063
1208 Abrol IP, Yadav JSP, Massoud FI. 1988. Salt-affected Soils and Their Management. Food & Agriculture
1209 Org.
1210 Ariel FD, Diet A, Crespi M, Chan RL. 2010. The LOB-like transcription factor MtLBD1 controls Medicago
1211 truncatula root architecture under salt stress. *Plant Signal Behav* **5**:1666–1668.
1212 doi:10.4161/psb.5.12.14020
1213 Asch F, Dingkuhn M, Sow A, Audebert A. 2005. Drought-induced changes in rooting patterns and
1214 assimilate partitioning between root and shoot in upland rice. *Field Crops Res* **93**:223–236.
1215 doi:10.1016/j.fcr.2004.10.002
1216 Awlia M, Alshareef N, Saber N, Korte A, Oakey H, Panzarová K, Trtílek M, Negrão S, Tester M, Julkowska
1217 MM. 2021. Genetic mapping of the early responses to salt stress in Arabidopsis thaliana. *Plant J*
1218 **107**:544–563. doi:10.1111/tpj.15310
1219 Awlia M, Nigro A, Fajkus J, Schmoeckel SM, Negrão S, Santelia D, Trtílek M, Tester M, Julkowska MM,
1220 Panzarová K. 2016. High-Throughput Non-destructive Phenotyping of Traits that Contribute to
1221 Salinity Tolerance in Arabidopsis thaliana. *Front Plant Sci* **7**:1414. doi:10.3389/fpls.2016.01414
1222 Bacher H, Sharaby Y, Walia H, Peleg Z. 2022. Modifying root-to-shoot ratio improves root water influxes
1223 in wheat under drought stress. *J Exp Bot* **73**:1643–1654. doi:10.1093/jxb/erab500
1224 Barberon M, Vermeer JEM, De Bellis D, Wang P, Naseer S, Andersen TG, Humbel BM, Nawrath C, Takano
1225 J, Salt DE, Geldner N. 2016. Adaptation of Root Function by Nutrient-Induced Plasticity of
1226 Endodermal Differentiation. *Cell* **164**:447–459. doi:10.1016/j.cell.2015.12.021
1227 Baxter I, Hosmani PS, Rus A, Lahner B, Borevitz JO, Muthukumar B, Mickelbart MV, Schreiber L, Franke
1228 RB, Salt DE. 2009. Root suberin forms an extracellular barrier that affects water relations and
1229 mineral nutrition in Arabidopsis. *PLoS Genet* **5**:e1000492. doi:10.1371/journal.pgen.1000492
1230 Beilstein MA, Renfrew KB, Song X, Shakirov EV, Zanis MJ, Shippen DE. 2015. Evolution of the Telomere-
1231 Associated Protein POT1a in Arabidopsis thaliana Is Characterized by Positive Selection to Reinforce
1232 Protein-Protein Interaction. *Mol Biol Evol* **32**:1329–1341. doi:10.1093/molbev/msv025
1233 Birnbaum K, Shasha DE, Wang JY, Jung JW, Lambert GM, Galbraith DW, Benfey PN. 2003. A gene
1234 expression map of the Arabidopsis root. *Science* **302**:1956–1960. doi:10.1126/science.1090022
1235 Brady SM, Zhang L, Megraw M, Martinez NJ, Jiang E, Yi CS, Liu W, Zeng A, Taylor-Teeples M, Kim D,
1236 Ahnert S, Ohler U, Ware D, Walhout AJM, Benfey PN. 2011. A stele-enriched gene regulatory
1237 network in the Arabidopsis root. *Mol Syst Biol* **7**:459. doi:10.1038/msb.2010.114
1238 Chen Q, Hu T, Li X, Song C-P, Zhu J-K, Chen L, Zhao Y. 2022. Phosphorylation of SWEET sucrose
1239 transporters regulates plant root:shoot ratio under drought. *Nat Plants* **8**:68–77.
1240 doi:10.1038/s41477-021-01040-7
1241 Clough SJ, Bent AF. 1998. Floral dip: a simplified method forAgrobacterium-mediated transformation
1242 ofArabidopsis thaliana. *Plant J* **16**:735–743. doi:10.1046/j.1365-313x.1998.00343.x
1243 Crain J, Larson S, Dorn K, Hagedorn T, DeHaan L, Poland J. 2020. Sequenced-based paternity analysis to
1244 improve breeding and identify self-incompatibility loci in intermediate wheatgrass (Thinopyrum
1245 intermedium). *Theor Appl Genet* **133**:3217–3233. doi:10.1007/s00122-020-03666-1
1246 Delude C, Vishwanath SJ, Rowland O, Domergue F. 2017. Root Aliphatic Suberin Analysis Using Non-
1247 extraction or Solvent-extraction Methods. *Bio-protocol* **7**. doi:10.21769/BioProtoc.2331
1248 Deolu-Ajayi AO, Meyer AJ, Haring MA, Julkowska MM, Testerink C. 2019. Genetic Loci Associated with
1249 Early Salt Stress Responses of Roots. *iScience* **21**:458–473. doi:10.1016/j.isci.2019.10.043
1250 Duan L, Dietrich D, Ng CH, Chan PMY, Bhalerao R, Bennett MJ, Dinneny JR. 2013. Endodermal ABA

signaling promotes lateral root quiescence during salt stress in Arabidopsis seedlings. *Plant Cell* **25**:324–341. doi:10.1105/tpc.112.107227

Fischer, G., Nachtergaele, O. F, Velthuizen V, T. H, Chiozza, F., Franceschini, G., Henry, M., Muchoney, D., Tramberend, S. 2021. Global Agro-Ecological Zones v4 – Model documentation. Food & Agriculture Org.

Foster KJ, Miklavcic SJ. 2017. A Comprehensive Biophysical Model of Ion and Water Transport in Plant Roots. I. Clarifying the Roles of Endodermal Barriers in the Salt Stress Response. *Front Plant Sci* **8**:1326. doi:10.3389/fpls.2017.01326

Fu Y, Yang Y, Chen S, Ning N, Hu H. 2019. Arabidopsis IAR4 Modulates Primary Root Growth Under Salt Stress Through ROS-Mediated Modulation of Auxin Distribution. *Front Plant Sci* **10**:522. doi:10.3389/fpls.2019.00522

Galvan-Ampudia CS, Julkowska MM, Darwish E, Gandullo J, Korver RA, Brunoud G, Haring MA, Munnik T, Vernoux T, Testerink C. 2013. Halotropism is a response of plant roots to avoid a saline environment. *Curr Biol* **23**:2044–2050. doi:10.1016/j.cub.2013.08.042

Gehan MA, Fahlgren N, Abbasi A, Berry JC, Callen ST, Chavez L, Doust AN, Feldman MJ, Gilbert KB, Hodge JG, Hoyer JS, Lin A, Liu S, Lizárraga C, Lorence A, Miller M, Platon E, Tessman M, Sax T. 2017. PlantCV v2: Image analysis software for high-throughput plant phenotyping. *PeerJ* **5**:e4088. doi:10.7717/peerj.4088

Geng Y, Wu R, Wee CW, Xie F, Wei X, Chan PMY, Tham C, Duan L, Dinneny JR. 2013. A spatio-temporal understanding of growth regulation during the salt stress response in Arabidopsis. *Plant Cell* **25**:2132–2154. doi:10.1105/tpc.113.112896

Guo W, Chen L, Herrera-Estrella L, Cao D, Tran L-SP. 2020. Altering Plant Architecture to Improve Performance and Resistance. *Trends Plant Sci* **25**:1154–1170. doi:10.1016/j.tplants.2020.05.009

Hassani A, Azapagic A, Shokri N. 2021. Global predictions of primary soil salinization under changing climate in the 21st century. *Nat Commun* **12**:6663. doi:10.1038/s41467-021-26907-3

Höfer R, Briesen I, Beck M, Pinot F, Schreiber L, Franke R. 2008. The Arabidopsis cytochrome P450 CYP86A1 encodes a fatty acid omega-hydroxylase involved in suberin monomer biosynthesis. *J Exp Bot* **59**:2347–2360. doi:10.1093/jxb/ern101

Horton MW, Hancock AM, Huang YS, Toomajian C, Atwell S, Auton A, Muliyati NW, Platt A, Sperone FG, Vilhjálmsson BJ, Nordborg M, Borevitz JO, Bergelson J. 2012. Genome-wide patterns of genetic variation in worldwide Arabidopsis thaliana accessions from the RegMap panel. *Nat Genet* **44**:212–216. doi:10.1038/ng.1042

Hu Y, Wu Q, Sprague SA, Park J, Oh M, Rajashekar CB, Koiwa H, Nakata PA, Cheng N, Hirschi KD, White FF, Park S. 2015. Tomato expressing Arabidopsis glutaredoxin gene AtGRXS17 confers tolerance to chilling stress via modulating cold responsive components. *Hortic Res* **2**:15051. doi:10.1038/hortres.2015.51

Hu Y, Zeng L, Lv X, Guo J, Li X, Zhang X, Wang D, Wang J, Bi J, Julkowska MM, Li B. 2023. NIGT1.4 maintains primary root elongation in response to salt stress through induction of ERF1 in Arabidopsis. *Plant J* **116**:173–186. doi:10.1111/tpj.16369

Julkowska MM, Hoefsloot HCJ, Mol S, Feron R, de Boer G-J, Haring MA, Testerink C. 2014. Capturing Arabidopsis root architecture dynamics with ROOT-FIT reveals diversity in responses to salinity. *Plant Physiol* **166**:1387–1402. doi:10.1104/pp.114.248963

Julkowska MM, Klei K, Fokkens L, Haring MA, Schranz ME, Testerink C. 2016. Natural variation in rosette size under salt stress conditions corresponds to developmental differences between Arabidopsis accessions and allelic variation in the LRR-KISS gene. *J Exp Bot* **67**:2127–2138. doi:10.1093/jxb/erw015

Julkowska MM, Koevoets IT, Mol S, Hoefsloot H, Feron R, Tester MA, Keurentjes JJB, Korte A, Haring MA, de Boer G-J, Testerink C. 2017. Genetic Components of Root Architecture Remodeling in Response

1299 to Salt Stress. *Plant Cell* **29**:3198–3213. doi:10.1105/tpc.16.00680
1300 Julkowska MM, Saade S, Agarwal G, Gao G, Pailles Y, Awlia M, Tester M. 2018. MVAPP—multivariate
1301 analysis application for streamlined data analysis and curation. *Plant Physiol* **23**:44.
1302 Julkowska MM, Testerink C. 2015. Tuning plant signaling and growth to survive salt. *Trends Plant Sci*
1303 **20**:586–594. doi:10.1016/j.tplants.2015.06.008
1304 Karcher DE, Richardson MD, Hignight K, Rush D. 2008. Drought tolerance of tall fescue populations
1305 selected for high root/shoot ratios and summer survival. *Crop Sci* **48**:771–777.
1306 doi:10.2135/cropsci2007.05.0272
1307 Kassambara A. n.d. ggpubr:'ggplot2'Based Publication Ready Plots. R package version 0.4. 0. *]*
1308 *https://cran-r-project org/web/packages/ggpubr/indes ….*
1309 Kondou Y, Noguchi K, Kutsuna S, Kawashima M, Yoneda A, Ishibashi M, Muto S, Ichikawa T, Nakazawa
1310 M, Matsui M, Manabe K. 2013. Overexpression of DWARF AND LESION FORMATION 1 (DLE1)
1311 causes altered activation of plant defense system in Arabidopsis thaliana. *Plant Biotechnol* **30**:385–
1312 392. doi:10.5511/plantbiotechnology.13.0605a
1313 Korver RA, van den Berg T, Meyer AJ, Galvan-Ampudia CS, Ten Tusscher KHWJ, Testerink C. 2020.
1314 Halotropism requires phospholipase Dζ1-mediated modulation of cellular polarity of auxin
1315 transport carriers. *Plant Cell Environ* **43**:143–158. doi:10.1111/pce.13646
1316 Kreszies T, Shellakkutti N, Osthoff A, Yu P, Baldauf JA, Zeisler-Diehl VV, Ranathunge K, Hochholdinger F,
1317 Schreiber L. 2019. Osmotic stress enhances suberization of apoplastic barriers in barley seminal
1318 roots: analysis of chemical, transcriptomic and physiological responses. *New Phytol* **221**:180–194.
1319 doi:10.1111/nph.15351
1320 Lampropoulos A, Sutikovic Z, Wenzl C, Maegele I, Lohmann JU, Forner J. 2013. GreenGate---a novel,
1321 versatile, and efficient cloning system for plant transgenesis. *PLoS One* **8**:e83043.
1322 doi:10.1371/journal.pone.0083043
1323 Laurie S, Feeney KA, Maathuis FJM, Heard PJ, Brown SJ, Leigh RA. 2002. A role for HKT1 in sodium
1324 uptake by wheat roots. *Plant J* **32**:139–149. doi:10.1046/j.1365-313x.2002.01410.x
1325 Lian X, Zhang S, Huang G, Huang L, Zhang J, Hu F. 2021. Confirmation of a Gametophytic Self-
1326 Incompatibility in Oryza longistaminata. *Front Plant Sci* **12**:576340. doi:10.3389/fpls.2021.576340
1327 Li B, Kamiya T, Kalmbach L, Yamagami M, Yamaguchi K, Shigenobu S, Sawa S, Danku JMC, Salt DE,
1328 Geldner N, Fujiwara T. 2017. Role of LOTR1 in Nutrient Transport through Organization of Spatial
1329 Distribution of Root Endodermal Barriers. *Curr Biol* **27**:758–765. doi:10.1016/j.cub.2017.01.030
1330 Li Y, Beisson F, Koo AJK, Molina I, Pollard M, Ohlrogge J. 2007. Identification of acyltransferases required
1331 for cutin biosynthesis and production of cutin with suberin-like monomers. *Proc Natl Acad Sci U S A*
1332 **104**:18339–18344. doi:10.1073/pnas.0706984104
1333 Lobet G, Pagès L, Draye X. 2011. A novel image-analysis toolbox enabling quantitative analysis of root
1334 system architecture. *Plant Physiol* **157**:29–39. doi:10.1104/pp.111.179895
1335 Lu K-K, Song R-F, Guo J-X, Zhang Y, Zuo J-X, Chen H-H, Liao C-Y, Hu X-Y, Ren F, Lu Y-T, Liu W-C. 2023.
1336 CycC1;1-WRKY75 complex-mediated transcriptional regulation of SOS1 controls salt stress
1337 tolerance in Arabidopsis. *Plant Cell* **35**:2570–2591. doi:10.1093/plcell/koad105
1338 Mäser P, Eckelman B, Vaidyanathan R, Horie T, Fairbairn DJ, Kubo M, Yamagami M, Yamaguchi K,
1339 Nishimura M, Uozumi N, Robertson W, Sussman MR, Schroeder JI. 2002. Altered shoot/root Na+
1340 distribution and bifurcating salt sensitivity in Arabidopsis by genetic disruption of the Na+
1341 transporter AtHKT1. *FEBS Lett* **531**:157–161. doi:10.1016/s0014-5793(02)03488-9
1342 Møller IS, Gilliham M, Jha D, Mayo GM, Roy SJ, Coates JC, Haseloff J, Tester M. 2009. Shoot Na+
1343 exclusion and increased salinity tolerance engineered by cell type-specific alteration of Na+
1344 transport in Arabidopsis. *Plant Cell* **21**:2163–2178. doi:10.1105/tpc.108.064568
1345 Munns R, Tester M. 2008. Mechanisms of Salinity Tolerance. *Annual Review of Plant Biology*.
1346 doi:10.1146/annurev.arplant.59.032607.092911

1347 Nelson ADL, Forsythe ES, Gan X, Tsiantis M, Beilstein MA. 2014. Extending the model of Arabidopsis
1348 telomere length and composition across Brassicaceae. *Chromosome Res* **22**:153–166.
1349 doi:10.1007/s10577-014-9423-y
1350 Nelson ADL, Haug-Baltzell AK, Davey S, Gregory BD, Lyons E. 2018. EPIC-CoGe: managing and analyzing
1351 genomic data. *Bioinformatics* **34**:2651–2653. doi:10.1093/bioinformatics/bty106
1352 Norris SR, Meyer SE, Callis J. 1993. The intron of Arabidopsis thaliana polyubiquitin genes is conserved in
1353 location and is a quantitative determinant of chimeric gene expression. *Plant Mol Biol* **21**:895–906.
1354 doi:10.1007/BF00027120
1355 Ramachandran P, Augstein F, Nguyen V, Carlsbecker A. 2020. Coping With Water Limitation: Hormones
1356 That Modify Plant Root Xylem Development. *Front Plant Sci* **11**:570. doi:10.3389/fpls.2020.00570
1357 Ranathunge K, Schreiber L. 2011. Water and solute permeabilities of Arabidopsis roots in relation to the
1358 amount and composition of aliphatic suberin. *J Exp Bot* **62**:1961–1974. doi:10.1093/jxb/erq389
1359 Richards LA. 1969. Diagnosis and Improvement of Saline and Alkali Soils. United States Department of
1360 Agriculture.
1361 Şekerci K, Higashitani N, Ozgur R, Uzilday B, Higashitani A, Turkan I. 2023. A stratagem for primary root
1362 elongation under moderate salt stress in the halophyte Schrenkiella parvula. *Physiol Plant*
1363 **175**:e13937. doi:10.1111/ppl.13937
1364 Shukla V, Han J-P, Cléard F, Lefebvre-Legendre L, Gully K, Flis P, Berhin A, Andersen TG, Salt DE, Nawrath
1365 C, Barberon M. 2021. Suberin plasticity to developmental and exogenous cues is regulated by a set
1366 of MYB transcription factors. *Proc Natl Acad Sci U S A* **118**. doi:10.1073/pnas.2101730118
1367 Stamatakis A. 2014. RAxML version 8: a tool for phylogenetic analysis and post-analysis of large
1368 phylogenies. *Bioinformatics* **30**:1312–1313. doi:10.1093/bioinformatics/btu033
1369 Team RC, Team MRC, Suggests M, Matrix S. 2018. Package stats. *The R Stats Package*.
1370 Uga Y, Sugimoto K, Ogawa S, Rane J, Ishitani M, Hara N, Kitomi Y, Inukai Y, Ono K, Kanno N, Inoue H,
1371 Takehisa H, Motoyama R, Nagamura Y, Wu J, Matsumoto T, Takai T, Okuno K, Yano M. 2013.
1372 Control of root system architecture by DEEPER ROOTING 1 increases rice yield under drought
1373 conditions. *Nat Genet* **45**:1097–1102. doi:10.1038/ng.2725
1374 Ursache R, De Jesus Vieira Teixeira C, Dénervaud Tendon V, Gully K, De Bellis D, Schmid-Siegert E, Grube
1375 Andersen T, Shekhar V, Calderon S, Pradervand S, Nawrath C, Geldner N, Vermeer JEM. 2021.
1376 GDSL-domain proteins have key roles in suberin polymerization and degradation. *Nat Plants* **7**:353–
1377 364. doi:10.1038/s41477-021-00862-9
1378 Valenzuela CE, Acevedo-Acevedo O, Miranda GS, Vergara-Barros P, Holuigue L, Figueroa CR, Figueroa
1379 PM. 2016. Salt stress response triggers activation of the jasmonate signaling pathway leading to
1380 inhibition of cell elongation in Arabidopsis primary root. *J Exp Bot* **67**:4209–4220.
1381 doi:10.1093/jxb/erw202
1382 Wang X, Zhang Y, Wang L, Pan Z, He S, Gao Q, Chen B, Gong W, Du X. 2020. Casparian strip membrane
1383 domain proteins in Gossypium arboreum: genome-wide identification and negative regulation of
1384 lateral root growth. *BMC Genomics* **21**:340. doi:10.1186/s12864-020-6723-9
1385 Wang Y, Meng B, Zhong S, Wang D, Ma J, Sun W. 2018. Aboveground biomass and root/shoot ratio
1386 regulated drought susceptibility of ecosystem carbon exchange in a meadow steppe. *Plant Soil*
1387 **432**:259–272. doi:10.1007/s11104-018-3790-7
1388 Weigel D, Mott R. 2009. The 1001 genomes project for Arabidopsis thaliana. *Genome Biol* **10**:107.
1389 doi:10.1186/gb-2009-10-5-107
1390 Wei T, Simko V. 2017. R package“ corrplot”: Visualization of a Correlation Matrix (Version 0.84). *Retrived*
1391 *from, https://github com/taiyun/corrplot*.
1392 West G, Inzé D, Beemster GTS. 2004. Cell cycle modulation in the response of the primary root of
1393 Arabidopsis to salt stress. *Plant Physiol* **135**:1050–1058. doi:10.1104/pp.104.040022
1394 Wilke CO. 2016. cowplot: streamlined plot theme and plot annotations for “ggplot2.” *CRAN Repos*.

1395 Wu SJ, Ding L, Zhu JK. 1996. SOS1, a Genetic Locus Essential for Salt Tolerance and Potassium
1396 Acquisition. *Plant Cell* **8**:617–627. doi:10.1105/tpc.8.4.617
1397 Xu W, Cui K, Xu A, Nie L, Huang J, Peng S. 2015. Drought stress condition increases root to shoot ratio via
1398 alteration of carbohydrate partitioning and enzymatic activity in rice seedlings. *Acta Physiol Plant*
1399 **37**. doi:10.1007/s11738-014-1760-0
1400 Yang Z. 2007. PAML 4: phylogenetic analysis by maximum likelihood. *Mol Biol Evol* **24**:1586–1591.
1401 doi:10.1093/molbev/msm088
1402 Yu L'ang, Sussman H, Khmelnitsky O, Ishka MR, Srinivasan A, Nelson ADL, Julkowska MM. 2023.
1403 Development of a mobile, high-throughput, and low-cost image-based plant growth phenotyping
1404 system. *bioRxiv*. doi:10.1101/2023.07.18.549560
1405 Yu B, Zheng W, Xing L, Zhu J-K, Persson S, Zhao Y. 2022. Root twisting drives halotropism via stress-
1406 induced microtubule reorientation. *Dev Cell* **57**:2412–2425.e6. doi:10.1016/j.devcel.2022.09.012
1407 Zarebanadkouki M, Trtik P, Hayat F, Carminati A, Kaestner A. 2019. Root water uptake and its pathways
1408 across the root: quantification at the cellular scale. *Sci Rep* **9**:12979. doi:10.1038/s41598-019-
1409 49528-9
1410 Zou Y, Gigli-Bisceglia N, van Zelm E, Julkowska MM, Zeng Y, Cheng Y, Koevoets IT, Jørgensen B, Giesbers
1411 M, Vroom J, Ketelaar T, Petersen BL, Zhang Y, Testerink C. 2022. Cell wall extensin arabinosylation is
1412 required for root directional response to salinity. *bioRxiv*. doi:10.1101/2022.06.22.497042
1413 Zou Y, Gigli-Bisceglia N, Zelm E, Kokkinopoulou P. 2022. Cell wall extensin arabinosylation is required for
1414 root directional response to salinity. *bioRxiv*.